Design and analytical evaluation of an impact-based four-point bending configuration for piezoelectric energy harvesting

Hasani, Milad; Khazaee, Majid; Huber, John E.; Rosendahl, Lasse; Rezania, Alireza

Published in:
Applied Energy

DOI (link to publication from Publisher):
10.1016/j.apenergy.2023.121461

Publication date:
2023

Document Version
Publisher's PDF, also known as Version of record

Applied Energy 347 (2023) 121461

Contents lists available at ScienceDirect

Applied Energy

journal homepage: www.elsevier.com/locate/apenergy

Design and analytical evaluation of an impact-based four-point bending configuration for piezoelectric energy harvesting

Milad Hasani [a], Majid Khazaee [a], John E. Huber [b], Lasse Rosendahl [a], Alireza Rezania [a,*]

[a] Department of Energy Technology, Aalborg University, Pontopidanstraede 111, 9220 Aalborg, Denmark
[b] Department of Engineerings Science, University of Oxford, Parks Rd, Oxford OX1 3PJ, United Kingdom

HIGHLIGHTS

- Electromechanical model with novel four-point bending configuration is derived.
- The model is validated by a finite element model and experimental results.
- This harvester significantly improves energy conversion efficiency by 322%.
- Modified stress distribution enhances normalized output energy by 638%.
- The configuration fulfils fatigue endurance and high energy conversion efficiency.

ARTICLE INFO

Keywords:
Piezoelectric energy harvesting
Ambient vibration
Impact excitation
Energy conversion efficiency

ABSTRACT

Aiming toward improved energy conversion in piezoelectric energy harvesters, this study investigates four-point bending (FPB) energy harvesters (FPB-EH) to explore their prominent features and characteristics. The FPB configuration innovatively extends energy harvesting capabilities relative to conventional cantilever beams. The FPB-EH comprises a composite piezoelectric beam that rests on two supports of a fixed clamp, excited by contact force applied at two contact lines on a moving clamp. A comprehensive analytical electromechanical model for the vibrating energy harvester is presented with unique modeling features, including multi-beam sections and multi-mode-shape functions. Solutions of the analytical model are presented for a wide range of contact force types, including steady-state solutions for harmonic forces, impact forces, periodic and non-periodic arbitrary forces. This comprehensive model progresses the state-of-the-art piezoelectric modeling knowledge and is readily applicable to various energy harvesting configurations. The model is validated against experimental results and finite element analysis. Next, a parametric study was performed to evaluate the effects of various FPB characteristics, including the fixed and moving clamp spans, the waveform, and the period-time of contact force. The results indicate that the FPB configuration can enhance energy conversion efficiency and normalized output energy by factors of over 3 and 6, respectively. Finally, guidance is given for selecting between cantilever and four-point bending configurations.

1. Introduction

The development of electronics technologies has decreased the energy consumption of electronic devices, enabling us to supply the required energy for low-powered devices in inaccessible areas through energy harvesting methods from environmental energy sources rather than conventional batteries [1]. The literature has explored several ambient energy sources for energy harvesting, including electromagnetic radiation, temperature difference, and mechanical vibration. Mechanical vibration has been realized as a sustainable ambient power source because of its accessibility in various environments and easy system integration [2]. In this way, various approaches based on mechanical vibration have been introduced, including electromagnetics [3,4], triboelectric [5,6], and piezoelectric [7,8].

The piezoelectric cantilever beams under base displacement excitation have been studied comprehensively in previous investigations as a prominent configuration in piezoelectric energy harvesting systems (PEHS). The strengths and weaknesses of this configuration were discussed frequently in the literature. The low power bandwidth of the

* Corresponding author.
E-mail address: alr@energy.aau.dk (A. Rezania).

https://doi.org/10.1016/j.apenergy.2023.121461
Received 17 October 2022; Received in revised form 6 April 2023; Accepted 11 June 2023
Available online 26 June 2023

Nomenclature

a_0	Mass proportional damping coefficient
a_1	Stiffness proportional damping coefficient
b	Beam width (m)
β	Dimensional variable regarding natural frequencies
$c_1, c_2, \ldots, c_8$	Constants of mode shape function
c_9, c_{10}	Constants of the temporal function
c_{11}^E	Young's modulus of the piezoceramic layer at constant electric field (GPa)
C_P	Equivalent capacitance of piezoelectric layer (F)
D_{33}	33-component of electric displacement matrix
E	Electric field on the piezoelectric layer (V/m)
E_{input}	Mechanical input energy
E_{output}	Electrical output energy
$\overline{\varepsilon_{33}}^S$	Permittivity constant (nF/m)
$\overline{e_{31}}$	Effective piezoelectric stress constant (C/m^2)
$\mathbb{F}$	Amplitude of harmonic force (N)
F_c	Equivalent generalized force
F_{trans}	Measured applied force to the force transducer (N)
$F_{inertia}$	Inertia force of the upper clamp (N)
F_{cont}	Contact force (N)
$\mathscr{F}_{cont}$	Laplace transform of F_{cont}
f_L	Lower frequency regarding bandwidth (Hz)
f_P	Peak frequency regarding bandwidth (Hz)
f_H	Higher frequency regarding bandwidth (Hz)
h	Layer thickness (m)
I	Second moment of area (m^4)
j	Unit imaginary number
j_P	Backward coupling term
K	Equivalent modal stiffness
L_b	Beam length (m)
L_d	Bottom clamp length (m)
L_{up}	Upper clamp length (m)
M	Equivalent modal mass
N	Number of harmonic pairs in Fourier series
q_i	Temporal part on separation of variables
q_{si}	Steady-state of temporal part expression
$\mathbb{Q}_i$	Amplitude of the temporal part's harmonic response
Q	Electric charge output of piezoelectric layer (C)
$\mathscr{Q}$	Laplace transform of Q
$\mathfrak{Q}$	Quality factor
RMS	Root mean square
s	Laplace variable
S	Mechanical strain (1)
T	Kinetic energy (J)
t	Time (s)
$\mathscr{T}$	Period-time of contact force
U	Strain potential energy (J)
v_s	Steady-state voltage expression
v	Output voltage of piezoelectric patch (V)
v_0	Initial condition of v
v_{imp}	Voltage expression per ideal impulse excitation
$\mathscr{V}$	Laplace transform of v
$\mathbb{V}$	Amplitude of the voltage's harmonic response
V	Material Volume (m^3)
w	Transversal displacement (m)
w_0	Initial value of displacement w
$\dot{w}_0$	Initial value of velocity $\dot{w}$
w_s	Steady-state displacement expression
$\mathbb{W}$	Amplitude of the displacement's harmonic response
$W_{i.e}$	Internal electrical energy (J)
W_{nc}	Virtual work of non-conservative forces (J)
x	Longitudinal direction in cartesian coordinate system xyz
$\mathscr{X}_i$	State space variables
y	Lateral direction in cartesian coordinate system xyz
Y	Young's modulus
z	Transverse direction in cartesian coordinate system xyz
γ	A positive constant parameter
δ	Variation operator
δ	Ideal unit impulse (Dirac delta function)
μ_i	Elements of the coefficient matrix
θ	Electromechanical coupling
ρ	Density (kg/m^3)
σ	Mechanical/electromechanical stress (Pa)
ϕ	Mode shape functions
ω	Natural frequency (rad/s)
ξ	Damping ratio

cantilever configuration leads to a narrow frequency band for matching base excitation with the harvester's principle natural frequency [3]. In this regard, nonlinearity characteristics have been used to address the drawback of narrow frequency bandwidth in linear PEHS [9,10]. Consequently, novel configurations of nonlinear PEHS were proposed to evaluate the effect of nonlinear dynamics with bi-stability and internal resonance characteristics [7,11,12]. Indeed, the nonlinear behavior improves bandwidth, which enables PEHS to generate more power from non-matched frequencies. In addition to nonlinear characteristics, some studies [9,13] have examined the PEHS under impact forces rather than harmonic excitation to deal with the bandwidth limitation. Indeed, impact excitation tackles the frequency matching limitation, providing an initial condition to PEHS with a short impact time [14], followed by free vibration for the rest of the motion time. This remarkable potential has encouraged the researcher to evaluate the impact of dissipation on PEHS based on Hertzian contact theory and the Hunt-Crossley model [9].

In addition to bandwidth restriction, the stress distribution over the length of a cantilever piezoelectric beam is not uniform; the strain is maximum around the clamped boundary and becomes zero at the free end [15]. Thus, the clamped areas generate the most power, leaving the majority of the harvesting beam volume ineffective. The high-stress zone around clamped boundary can threaten the operation of a harvester for long-term employment due to fatigue. Therefore, two approaches can be taken for stress distribution improvement: the material/structural approach and the boundary condition approach. Tailoring the harvester stiffness by fiber orientation has been proposed for composite piezoelectric harvesters [16]. Other options include tailoring the location of the piezoelectric material [17], strain-engineered material, auxetic multiple-rotating-cube substrate [18], and auxetic properties of the piezoelectric material [19]. For the boundary condition approach, poling direction [20], bistable [21,22], and clamped–clamped beams with a center mass [18,23] have also proven effective.

Much energy harvesting literature for power generation improvements is devoted to material advancements or PEHS structure modifications. The resulting materials and designs are complex and not commercially available. Finding a straightforward approach to enhance PEHS energy generation remains a critical unmet goal. Thus, this research emphasizes the use of an alternative boundary condition as a route to better PEHS performance, not requiring sophisticated material development. This study proposes and explores the four-point bending boundary condition (FPB-BC) for PEHs. The FPB-BC facilitates the relative uniformity of stress/strain distribution over the harvester's surface, which enhances the harvester's performance. Thus, the FPB-BC has potential for better power generation, material usage, and longer fatigue life.

The current research develops a comprehensive analytical model for piezoelectric beams under the FPB-BC. The advanced multi-sectional beam model considers harmonic, impact, periodic, and non-periodic excitation forces. The proposed model extends the current single continuous piezoelectric beam model to advanced multi-sectional FPB-BC. Hamiltonian and Euler–Bernoulli beam theories are utilized to implement a powerful and flexible analytical framework. The proposed model considers a multi-sectional harvester; a robust multi-sectional modal analysis is accomplished by two independent model shape functions and eigenvalue relations, which enable us to predict the harvester's response once the beam length is higher than the fixed clamp span. The electromechanical model is employed in a parameter study to find the optimal conditions. The best performance of FPB-EH is evaluated in terms of force waveform and the geometrical parameters, indicating its capabilities regarding enhanced frequency bandwidth and power generation level. Moreover, the FPB-EH's weaknesses and strengths are compared against cantilever PEHs. From a practical point of view, this study provides guidelines to determine which configuration type (between FPB and cantilevered harvester ones) is appropriate for a specific application.

The key contribution of this study is the enhancement of energy generation, improving the long-term working of PEHS, and efficient material usage. The study indicates guidelines for more efficient harvesting systems. The work of this paper is organized as follows. Section 2 introduces the design configuration of an FPB-EH, which includes two clamps and a piezoelectric beam. Section 3 develops an electromechanical model to predict the harvester output. In addition, the governing differential equations are solved through the Laplace Transform, and a Fourier series solution is implemented into Frequency Response Functions (FRFs) to find the steady-state response for an arbitrary periodic excitation. Section 4 describes the experimental setup of an FPB-EH, and Section 5 validates the proposed model against both experimental results and FEM outputs (COMSOL Multiphysics) based on the transient and steady-state responses. Moreover, a parametric study explores the effects of different harvester characteristics on performance. Conclusions are given in Section 6.

2. Design configuration

The configuration of an FPB-EH is illustrated in Fig. 1. This configuration consists of a multilayer piezoelectric beam (MPB) and two clamp clips on the upper and lower sides of the MPB. The MPB comprises two active piezoelectric layers (PZT-5A) and a middle substrate layer (brass), which are bonded together. The MPB is constrained through the bottom clamp clip, which can be considered as a roller support, provided the slip friction is negligible. The upper clamp clip is connected to the force transducer of an impact hammer for applying an impulse excitation to the MPB through two contacts. It should be noted that the centerlines of the MPB, upper and lower clamps are aligned. Therefore, the applied forces through the two legs are identical due to the system symmetry relative to the y-z plane, as shown in Fig. 3. Besides, this symmetry enables us to study half of the harvester instead of the whole in section 3.

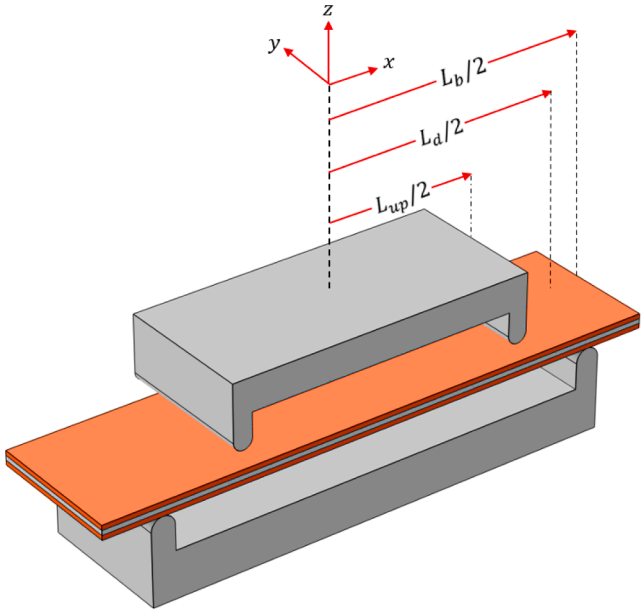

Fig. 1. The schematic of the FPB configuration.

The piezoelectric layers are poled along the z-axis, as shown in Fig. 2-a. The longitudinal stress/strain of the upper and lower piezoelectric layers have opposite directions during a pure bending motion due to their position relative to the neutral axis. As a result, the generated electric field of two active layers and parallel electrical connection can be shown in Fig. 2-b.

3. Analytical model

The Hamiltonian method and Euler–Bernoulli beam theory are employed to develop an electromechanical analytical model for the FPB configuration. The length-to-thickness ratio is assumed to be relatively large, so shear deformation and rotary inertia effects are negligible. Nonlinearity can be significant under high-level impact force, which leads to large deformation and geometric nonlinearity. In addition, the contact region extends from single point to the surface (within contact time) based on Hertz's contact theory, consequently, the contact stiffness (contact elasticity) is nonlinear and contact-surface dependent [24]. To focus mainly on the energy harvesting performance of this new piezoelectric setup, this study focuses on conditions that are not affected by geometric nonlinearity due to low impact force. This simplification enables us to provide a comprehensive analytical model of FPB-EH under impact excitation in the following.

The extended Hamilton's principle for an electromechanical system can be written as Eq. (1).

$$\int_{t_1}^{t_2} (\delta T - \delta U + \delta W_{i.e} + \delta W_{nc})\, dt = 0 \tag{1}$$

In the following, the total kinetic, potential, and internal electrical energies and the virtual work of non-conservative forces (mechanical and electric charge components) are expressed to develop the constitutive equations. The longitudinal stress based on the Euler-Bernoulli theory and plane-stress assumption is given by:

$$S_x(x,t) = -z\hat{w}(x)\ddot{} \tag{2}$$

In this article, the superscripts $\hat{}$ and $\dot{}$ denote the spatial and time derivatives, respectively. The longitudinal stress on the substrate and piezoelectric layers is expressed as:

$$\sigma_{sx}(x,t) = Y_s S_x(x,t) \tag{3}$$

$$\sigma_{Px}(x,t) = c_{11}^{E} S_x(x,t) - \overline{e_{31}} E_z(t) \tag{4}$$

The subscripts P and s present that this parameter is associated with piezoelectric and substrate layers, respectively. It is assumed that the electric field on the piezoelectric layers along the z-direction is uniform, which is described as:

$$E_z(t) = \frac{v(t)}{h_p} \tag{5}$$

The strain potential energy of the substrate layer and electromechanical energy of piezoelectric layers are calculated as Eq. (6) and Eq. (7), respectively.

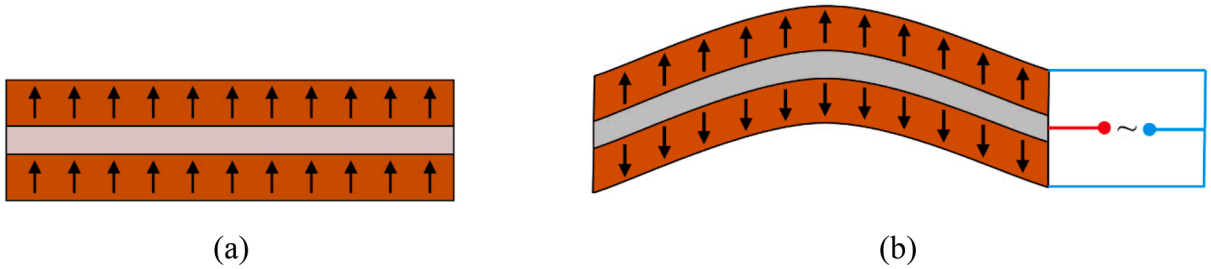

Fig. 2. The direction of (a) poling and (b) the electric field of MPB.

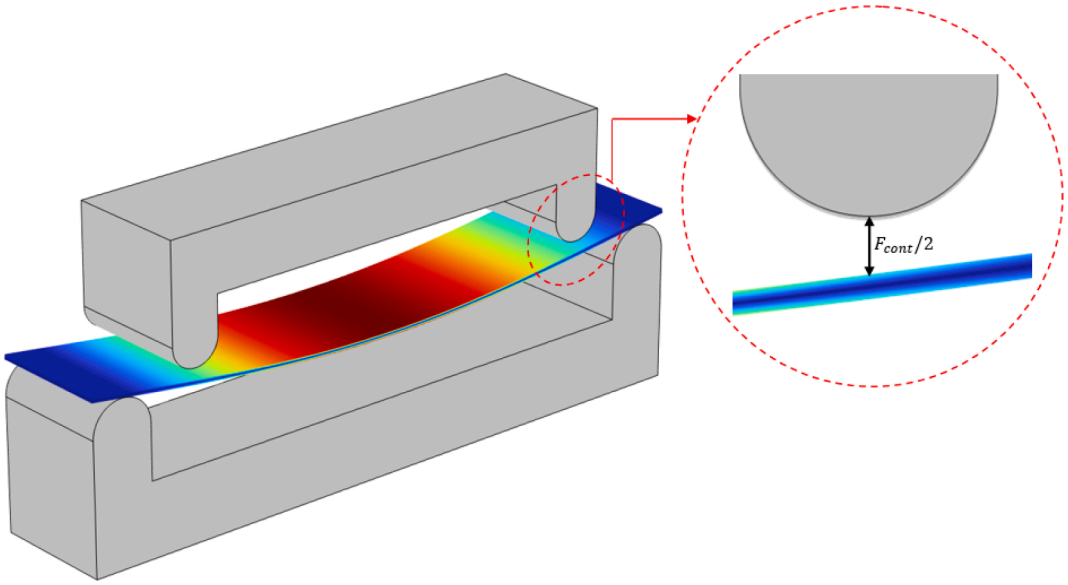

Fig. 3. The schematic of the contact force applied on MPB.

$$U_s = \frac{1}{2}\int_{V_s} \sigma_{s_x} S_x dV_s = \frac{Y_s I_s}{2}\int_{-\frac{L_b}{2}}^{\frac{L_b}{2}} w(x)^{''2} dx \tag{6}$$

$$U_P = \frac{1}{2}\int_{V_P} \sigma_{P_x} S_x dV_P = \frac{1}{2}\left[c_{11}^E I_P \int_{-\frac{L_b}{2}}^{\frac{L_b}{2}} w(x)^{''2} dx - j_P \left(\int_{-\frac{L_b}{2}}^{\frac{L_b}{2}} w(x)^{''} dx\right) v(t)\right] \tag{7}$$

where the backward coupling term is presented as

$$j_P = \frac{\overline{e}_{31}}{h_P} b\left(\left(\frac{h_s}{2}+h_P\right)^2 - \left(\frac{h_s}{2}\right)^2\right) \tag{8}$$

The piezoelectric layers' area moment of inertia can be written as

$$I_P = \frac{2}{3} b\left(\left(\frac{h_s}{2}+h_P\right)^3 - \left(\frac{h_s}{2}\right)^3\right) \tag{9}$$

In addition, the total kinetic energy comprises the kinetic energy of the substrate and piezoelectric layers, which are stated as:

$$T_s = \frac{1}{2}\int_{V_s} \rho_s \dot{w}(x)^2 dV_s = \frac{1}{2}\rho_s b h_s \int_{-\frac{L_b}{2}}^{\frac{L_b}{2}} \dot{w}(x)^2 dx \tag{10}$$

$$T_P = \frac{1}{2}\int_{V_P} \rho_P \dot{w}(x)^2 dV_P = \rho_P b h_s \int_{-\frac{L_b}{2}}^{\frac{L_b}{2}} \dot{w}(x)^2 dx \tag{11}$$

The total internal electrical energy of the piezoelectric layers is represented as:

$$W_{i.e} = \frac{1}{2}\int_V E_z D_{33} dV \tag{12}$$

The 3-component of the electric displacement vector is expressed as:

$$D_{33} = \overline{e_{31}}\sigma_{Px} + \overline{e_{33}}^s E_z \tag{13}$$

Separation of variables is utilized to separate the presented equations into spatial and temporal parts, with the transversal displacement expressed by

$$w(x,t) = \sum_{i=1}^{\infty} \phi_i(x) q_i(t) \tag{14}$$

So, the total kinetic, potential, and internal electrical energies are rewritten as Eqs. (15), (16), and (17), respectively:

$$T = \frac{1}{2}(\rho_b h_b + 2\rho_P h_P) b \sum_{i=1}^{\infty}\left[\int_{-\frac{L_b}{2}}^{\frac{L_b}{2}} \phi_i^2(x) dx \dot{q}_i^2(t)\right] \tag{15}$$

$$U=\frac{1}{2}\left(Y_sI_s+C_{11}^{E}I_P\right)\sum_{i=1}^{\infty}\left[\int_{-\frac{L_b}{2}}^{\frac{L_b}{2}}\phi_i^{''}(x)^2dxq_i^2(t)\right]+\sum_{i=1}^{\infty}\left[\frac{-1}{2}\int_{-\frac{L_b}{2}}^{\frac{L_b}{2}}j_p(x)\phi_i^{''}(x)dx\right]v(t)q_i(t) \tag{16}$$

$$W_{i.e}=\frac{1}{2}j_P\sum_{i=1}^{\infty}\left[\int_{-\frac{L_b}{2}}^{\frac{L_b}{2}}\phi_i^{''}(x)dxq_i(t)\right]v(t)+\frac{1}{2}C_Pv^2(t) \tag{17}$$

where the MPB's equivalent capacitance C_P is given by

$$C_P=\frac{2\overline{e_{33}}^{s}}{h_p}bL_b \tag{18}$$

The mechanical contact force is considered a non-conservative force, which is shown in Fig. 3 in more detail.

The variation of non-conservative virtual work due to contact force is then given by:

$$\delta W_{n.c.m}=\sum_{i=1}^{\infty}F_{cont}(t)\phi_i(x)|_{x=\frac{L_{up}}{2}}\delta q_i(t) \tag{19}$$

In addition, the variation of non-conservative virtual work of electric charge output $Q(t)$ is given by Eq. (20).

$$\delta W_{n.c.e}=Q(t)\delta v(t) \tag{20}$$

By substituting these expressions in Eq. (1), the extended Hamilton's principle leads to the following electromechanical Lagrange equations.

$$\frac{d}{dt}\left(\frac{\partial T}{\partial\dot{q}_i}\right)-\frac{\partial T}{\partial q_i}+\frac{\partial U}{\partial q_i}-\frac{\partial W_{ie}}{\partial q_i}=F_{cont}(t)\phi_i(x)|_{x=\frac{L_{up}}{2}} \tag{21}$$

$$\frac{d}{dt}\left(\frac{\partial T}{\partial\dot{v}}\right)-\frac{\partial T}{\partial v}+\frac{\partial U}{\partial v}-\frac{\partial W_{ie}}{\partial v}=Q(t) \tag{22}$$

The first electromechanical equation can be derived from Eq. (21) as:

$$M_i\ddot{q}_i(t)+k_iq_i(t)-\theta_iv(t)=F_{ci}(t) \tag{23}$$

The equivalent modal mass, stiffness, electromechanical coupling, and generalized force are introduced as follows:

$$M_i=\left(\rho_bh_b+\rho_ph_p\right)b\int_{-\frac{L_b}{2}}^{\frac{L_b}{2}}\phi_i^2(x)dx \tag{24}$$

$$K_i=\left(Y_sI_s+c_{11}^{E}I_P\right)\int_{-\frac{L_b}{2}}^{\frac{L_b}{2}}\phi_i^{''}(x)\,dx=2\left(Y_sI_s+c_{11}^{E}I_P\right)\left(\phi_i^{'}(x)\,|_{x=\frac{L_b}{2}}\right) \tag{25}$$

$$\theta_i=j_p\int_{-\frac{L_b}{2}}^{\frac{L_b}{2}}\phi_i^{''}(x)\,dx=2j_p\left(\phi_i^{'}(x)\,|_{x=\frac{L_b}{2}}\right) \tag{26}$$

$$F_{ci}(t)=F_{cont}(t)\,\phi_i(x)|_{x=\frac{L_{up}}{2}} \tag{27}$$

The first electromechanical equation is rewritten by normalization with respect to equivalent modal mass and adding Rayleigh damping as

$$\ddot{q}_i(t)+2\xi_i\omega_i\dot{q}_i(t)+\omega_i^2q_i(t)-\theta_iv(t)=f_{ci}(t) \tag{28}$$

In addition, the second electromechanical equation is developed based on Eq. (22) as

$$C_P\dot{v}(t)+\frac{v(t)}{R}+\sum_{i=1}^{\infty}\theta_i\dot{q}_i(t)=0 \tag{29}$$

The following section investigates the modal analysis for an MPB with roller boundary conditions.

3.1. Modal analysis

The modal analysis for linear transverse vibration is performed based on the described roller boundary condition regardless of piezoelectric effect and damping. The governing equation of an Euler-Bernoulli beam with uniform width under undamped free vibration can be expressed as [14]

$$\frac{\partial^4w(x,t)}{\partial x^4}+\frac{m}{YI}\frac{\partial^2w(x,t)}{\partial t^2}=0 \tag{30}$$

Using separation of variables, based on spatial and temporal functions [25],

$$\frac{d^4\phi(x)}{dx^4}-\gamma\frac{m}{YI}\phi(x)=0 \tag{31}$$

$$\frac{d^2\eta(t)}{dt^2}+\gamma\eta(t)=0 \tag{32}$$

Where γ is a positive constant parameter. Moreover, the boundary conditions for a symmetric beam (as shown in Fig. 1) can be written as

$$\left.\frac{\partial\phi(x,t)}{\partial x}\right|_{x=0}=0 \tag{33}$$

$$\left.\frac{\partial^3\phi(x,t)}{\partial x^3}\right|_{x=0}=0 \tag{34}$$

$$\phi\left(x=\frac{L_d}{2},t\right)=0 \tag{35}$$

$$\left.\frac{\partial^2\phi(x,t)}{\partial x^2}\right|_{x=\frac{L_b}{2}}=0 \tag{36}$$

$$\left.\frac{\partial^3\phi(x,t)}{\partial x^3}\right|_{x=\frac{L_b}{2}}=0 \tag{37}$$

Besides, the beam slope and curvature are identical at roller supports, which leads to two additional rational boundary conditions:

$$\left.\frac{\partial^2\phi_{in}(x)}{\partial x^2}\right|_{x=\frac{L_d}{2}}=\left.\frac{\partial^2\phi_{out}(x)}{\partial x^2}\right|_{x=\frac{L_d}{2}} \tag{38}$$

$$\left.\frac{\partial\phi_{in}(x)}{\partial x}\right|_{x=\frac{L_d}{2}}=\left.\frac{\partial\phi_{out}(x)}{\partial x}\right|_{x=\frac{L_d}{2}} \tag{39}$$

These distinct boundary condition expressions correspond to two separate internal and external sections shown in Fig. 4.

As a result, two shape functions are considered for the solution of the ordinary differential equation (ODE) expressed in Eq. (31) as:

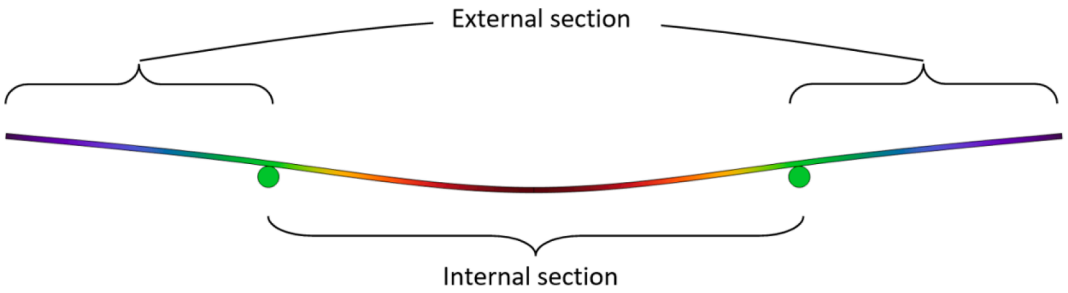

Fig. 4. The internal and external sections of MPB.

$$\phi(x)=\begin{cases}\phi_{in}(x)=c_1\sin(\beta x)+c_2\cos(\beta x)+c_3\sinh(\beta x)+c_4\cosh(\beta x), & -\dfrac{L_d}{2}\le x\le\dfrac{L_d}{2}\\ \phi_{ex}(x)=c_5\sin(\beta x)+c_6\cos(\beta x)+c_7\sinh(\beta x)+c_8\cosh(\beta x), & \dfrac{L_d}{2}<|x|<\dfrac{L_b}{2}\end{cases} \tag{40}$$

In addition, the solution of ODE regarding temporal function is given by:

$$\eta(t)=c_9\sin(\omega t)+c_{10}\cos(\omega t) \tag{41}$$

The ω is the natural frequency, which is defined as follows.

$$\omega=\beta^2\sqrt{\frac{YI}{m}} \tag{42}$$

By applying the boundary conditions Eq. (33) and Eq. (34)

$$c_1=c_3=0 \tag{43}$$

In addition, the remaining boundary conditions lead to a homogeneous system of linear equations represented in the matrix form as

$$\begin{bmatrix}\mu_7 & \mu_5 & 0 & 0 & 0 & 0\\ 0 & 0 & \mu_6 & \mu_7 & \mu_8 & \mu_5\\ \mu_6 & -\mu_8 & \mu_7 & -\mu_6 & \mu_5 & \mu_8\\ \mu_7 & -\mu_5 & -\mu_6 & -\mu_7 & \mu_8 & \mu_5\\ 0 & 0 & -\mu_2 & -\mu_4 & \mu_1 & \mu_3\\ 0 & 0 & -\mu_4 & \mu_2 & \mu_3 & \mu_1\end{bmatrix}\begin{Bmatrix}c_2\\ c_4\\ c_5\\ c_6\\ c_7\\ c_8\end{Bmatrix}=\begin{Bmatrix}0\\ 0\\ 0\\ 0\\ 0\\ 0\end{Bmatrix} \tag{44}$$

Where

$$\mu_1=\sinh\left(\frac{\beta L_b}{2}\right),\ \mu_2=\sin\left(\frac{\beta L_b}{2}\right)$$

$$\mu_3=\cosh\left(\frac{\beta L_b}{2}\right),\ \mu_4=\cos\left(\frac{\beta L_b}{2}\right) \tag{45}$$

$$\mu_5=\cosh\left(\frac{\beta L_d}{2}\right),\ \mu_6=\sin\left(\frac{\beta L_d}{2}\right)$$

$$\mu_7=\cos\left(\frac{\beta L_d}{2}\right),\ \mu_8=\sinh\left(\frac{\beta L_d}{2}\right)$$

The coefficient matrix should be singular in order to derive non-trivial solutions for this system. Therefore, the characteristic equation of this eigenvalue problem is given by the coefficient matrix's determinant as follows.

$$\begin{aligned}&(2\mu_2\mu_1-2\mu_4\mu_3){\mu_7}^2+(-4\mu_5-2\mu_4\mu_6\mu_1-2\mu_3\mu_6\mu_2)\mu_7-2\mu_5(\mu_5(\mu_4\mu_3\\&+\mu_2\mu_1)-\mu_8(\mu_4\mu_1+\mu_3\mu_2))\\&=0\end{aligned} \tag{46}$$

The characteristic equation has infinite positive roots representing eigenfrequencies of the harvester. Let β_n indicate the eigenvalue of the nth vibration mode associated with nth non-trivial eigenfunction:

$$\phi_n(x)=\begin{cases}c_{2,n}\left[\cos(\beta_n x)+\kappa_{42,n}\cosh(\beta_n x)\right], & -\dfrac{L_d}{2}\le x\le\dfrac{L_d}{2}\\ c_{2,n}\left[\kappa_{52,n}\sin(\beta_n x)+\kappa_{62,n}\cos(\beta_n x)+\kappa_{72,n}\sinh(\beta_n x)+\kappa_{82,n}\cosh(\beta_n x)\right], & \dfrac{L_d}{2}<|x|<\dfrac{L_b}{2}\end{cases} \tag{47}$$

Where

$$\kappa_{42,n}=\frac{-\mu_{7,n}}{\mu_{5,n}}$$

$$\kappa_{82,n}=-\frac{\mu_{2,n}\mu_{7,n}^2+\left(\mu_{1,n}\mu_{5,n}-\mu_{4,n}\mu_{6,n}\right)\mu_{7,n}+\mu_{4,n}\mu_{8,n}\mu_{5,n}}{\mu_{5,n}\left(\mu_{1,n}\mu_{5,n}-\mu_{4,n}\mu_{6,n}+\mu_{2,n}\mu_{7,n}-\mu_{3,n}\mu_{8,n}\right)}$$

$$\kappa_{72,n}=-\frac{\mu_{5,n}\kappa_{82,n}+\mu_{7,n}}{\mu_{8,n}} \tag{48}$$

$$\kappa_{62,n}=\frac{1}{\mu_{5,n}}\Big(\left(\kappa_{72,n}\mu_{6,n}-\kappa_{82,n}\right)\mu_{5,n}^2+\Big(-\kappa_{72,n}\mu_{7,n}\mu_{8,n}+\kappa_{82,n}\mu_{6,n}\mu_{8,n}-\mu_{7,n}^2+1\Big)\mu_{5,n}+\mu_{7,n}\mu_{8,n}\mu_{6,n}\Big)$$

$$\kappa_{52,n} = -\frac{\mu_{7,n}\kappa_{62,n} + \mu_{8,n}\kappa_{72,n} + \mu_{5,n}\kappa_{82,n}}{\mu_{6,n}}$$

Moreover,

$$\mu_{1,n} = \sinh\left(\frac{\beta_n L_b}{2}\right),\ \mu_{2,n} = \sin\left(\frac{\beta_n L_b}{2}\right)$$

$$\mu_{3,n} = \cosh\left(\frac{\beta_n L_b}{2}\right),\ \mu_{4,n} = \cos\left(\frac{\beta_n L_b}{2}\right) \quad (49)$$

$$\mu_{5,n} = \cosh\left(\frac{\beta_n L_d}{2}\right),\ \mu_{6,n} = \sin\left(\frac{\beta_n L_d}{2}\right)$$

$$\mu_{7,n} = \cos\left(\frac{\beta_n L_d}{2}\right),\ \mu_{8,n} = \sinh\left(\frac{\beta_n L_d}{2}\right)$$

Due to the orthogonality of the eigenfunctions, the coefficient $c_{2,n}$ can be determined through the mass normalization procedure described as

$$\int_{-\frac{L_b}{2}}^{\frac{L_b}{2}} \phi_n(x) m \phi_m(x) dx = \delta_{nm} \quad (50)$$

It should be mentioned that the expression of natural frequency in Eq. (42) can be extended for different vibration modes as follows

$$\omega_n = \beta_n^2 \sqrt{\frac{YI}{m}} \quad (51)$$

Even though the analytical equations of the developed model are relatively complicated, the characteristic and eigenfunctions expressions can be simplified regarding the specific condition $L_d = L_b$ as follows.

$$cos\left(\frac{\beta_n L_d}{2}\right) = 0\ ,\ \text{so}\ \beta_n = \frac{(2n-1)\pi}{L_d} n = 1, 2, 3, \cdots \quad (52)$$

$$\phi_n(x) = c_{2,n}\left[\cos(\beta_n x) + \kappa_{42,n}\cosh(\beta_n x)\right] \quad (53)$$

Therefore, the presented expressions for eigenvalue (Eq. (46)) and eigenfunction (Eq. (47)) can be utilized for solving differential equations Eq. (28) and Eq. (29) in the following section.

3.2. The electromechanical response under different excitation types

This section provides the electromechanical response of an MPB by solving the differential equations for various excitation types in the frequency and time domains.

3.2.1. The steady-state response for harmonic excitation in frequency space

In the first step, the harvester's steady-state response is investigated under harmonic excitation. In this way, the Laplace transform is applied to Eq. (28) and Eq. (29) as

$$\mathscr{C}_i(s)\left[s^2 + 2\xi_i\omega_i s + \omega_i^2\right] - \mathscr{V}(s)[\theta_i] = \mathscr{F}_{cont}(s)\phi_i(x)|_{x=\frac{L_{up}}{2}} \quad (54)$$

$$\mathscr{V}(s)\left[C_p s + \frac{1}{R}\right] + s\sum_{i=1}^{\infty}\theta_i\mathscr{C}_i(s) = 0 \quad (55)$$

The variables $\mathscr{C}_i(s)$ and $\mathscr{V}(s)$ can be extracted as

$$\mathscr{C}_i(s) = \left(\phi_i(x)|_{x=\frac{L_{up}}{2}} + \theta_i\left[\frac{-\sum_{i=1}^{\infty}\frac{\theta_i s\phi_i(x)|_{x=\frac{L_{up}}{2}}}{s^2+2\xi_i\omega_i s+\omega_i^2}}{C_p s + \frac{1}{R} + \sum_{i=1}^{\infty}\frac{\theta_i^2 s}{s^2+2\xi_i\omega_i s+\omega_i^2}}\right]\right)\frac{\mathscr{F}_{cont}(s)}{s^2+2\xi_i\omega_i s+\omega_i^2} \quad (56)$$

$$\mathscr{V}(s) = \mathscr{F}_{cont}(s)\left(\frac{-\sum_{i=1}^{\infty}\frac{\theta_i s\phi_i(x)|_{x=\frac{L_{up}}{2}}}{s^2+2\xi_i\omega_i s+\omega_i^2}}{C_p s + \frac{1}{R} + \sum_{i=1}^{\infty}\frac{\theta_i^2 s}{s^2+2\xi_i\omega_i s+\omega_i^2}}\right) \quad (57)$$

The harmonic contact force $F_{cont}(t) = \mathbb{F}e^{j\omega t}$ leads to the steady-state harmonic response $q_i(t) = \mathbb{Q}_i e^{j\omega t}$ and $v(t) = \mathbb{V}e^{j\omega t}$. For this aim, the steady-state responses can be given by $q_{si}(t) = \mathscr{C}_i(j\omega)e^{j\omega t}$ and $v_s(t) = \mathscr{V}(j\omega)e^{j\omega t}$ as [26]

$$q_{si}(\omega,t) = \left(\phi_i(x)|_{x=\frac{L_{up}}{2}} + \theta_i\left[\frac{-\sum_{i=1}^{\infty}\frac{j\theta_i\omega\phi_i(x)|_{x=\frac{L_{up}}{2}}}{-\omega^2+2j\xi_i\omega_i\omega+\omega_i^2}}{jC_p\omega + \frac{1}{R} + \sum_{i=1}^{\infty}\frac{j\theta_i^2\omega}{-\omega^2+2j\xi_i\omega_i\omega+\omega_i^2}}\right]\right)\frac{\mathbb{F}}{-\omega^2+2j\xi_i\omega_i\omega+\omega_i^2}e^{j\omega t} \quad (58)$$

$$v_s(\omega,t) = \mathbb{F}\left(\frac{-\sum_{i=1}^{\infty}\frac{j\theta_i\omega\phi_i(x)|_{x=\frac{L_{up}}{2}}}{-\omega^2+2j\xi_i\omega_i\omega+\omega_i^2}}{j\omega C_p + \frac{1}{R} + \sum_{i=1}^{\infty}\frac{j\theta_i^2\omega}{-\omega^2+2j\xi_i\omega_i\omega+\omega_i^2}}\right)e^{j\omega t} \quad (59)$$

In addition, the steady-state displacement expression is presented as $w_s(x,t) = \sum_{i=1}^{\infty}\mathbb{W}_i(x,t)$, where can be rewritten as

$$w_s(x,t)=\sum_{i=1}^{\infty}\left(\phi_i(x)|_{x=\frac{L_{up}}{2}}+\theta_i\left[\frac{-\sum_{i=1}^{\infty}\frac{j\vartheta_i\omega\phi_i(x)|_{x=\frac{L_{up}}{2}}}{-\omega^2+2j\xi_i\omega_i\omega+\omega_i^2}}{jC_p\omega+\frac{1}{R}+\sum_{i=1}^{\infty}\frac{j\vartheta_i^2\omega}{-\omega^2+2j\xi_i\omega_i\omega+\omega_i^2}}\right]\right)\frac{\mathbb{F}\phi_i(x)}{-\omega^2+2j\xi_i\omega_i\omega+\omega_i^2}e^{j\omega t} \tag{60}$$

This steady-state response is applicable to harmonic excitations but not to the analysis of system behavior under arbitrary inputs. In addition, the contact force may generally have an arbitrary form. Therefore, the following section focuses on a time-domain solution for an arbitrary excitation.

3.2.2. The time-dependent response for ideal impulse excitation

The derived transfer functions Eq. (56) and Eq. (57) can be employed to study the system's time-dependent response under various excitations with zero initial values. It is evident that the prediction of the time-dependent response is more complicated than the steady-state one. So, firstly, we evaluate the harvester's response under an ideal unit impulse excitation as given by Eq. (61) to determine the system response for more complicated input functions [14].

$$(t-a)=0 \quad \text{for} \quad t\neq a \tag{61}$$

$$\int_{t=-\infty}^{t=+\infty}\hat{1}(t-a)\,dt=1$$

As a result, the Laplace transform of ideal impulse force δ(t) becomes $\mathscr{T}_{cont}(s)=1$. The Laplace inverse of Eq. (57) should be derived for the representation of voltage expression in the time domain as follows.

$$v_{imp}(t)=\mathscr{L}^{-1}\left[\frac{-\sum_{i=1}^{\infty}\frac{\theta_i s\phi_i(x)|_{x=\frac{L_{up}}{2}}}{s^2+2\xi_i\omega_i s+\omega_i^2}}{C_p s+\frac{1}{R}+\sum_{i=1}^{\infty}\frac{\theta_i^2 s}{s^2+2\xi_i\omega_i s+\omega_i^2}}\right] \tag{62}$$

It should be mentioned that the parametric presentation regarding the Laplace inverse of this transfer function is not straightforward due to the series expansions. Therefore, it is expedient to perform the Laplace inverse only after substituting specific values into the variables of Eq. (62). Additionally, a numerical framework based on the state-space representation is provided in Section 3.2.4.

3.2.3. The steady-state response for arbitrary periodic excitation (Fourier expansion method)

In the following, the voltage and displacement solutions for arbitrary periodic excitation are parametrically represented based on the Fourier series. The general periodic excitation force with period-time $\mathscr{T}$ is defined as:

$$F_{cont}(t+\mathscr{T})=F_{cont}(t) \tag{63}$$

The periodic force can be represented by the Fourier series

$$F_{cont}(t)=\sum_{k=-\infty}^{\infty}\left[C_k e^{\left(\frac{2jk\pi t}{\mathscr{T}}\right)}\right] \tag{64}$$

where,

$$C_k=\frac{1}{\mathscr{T}}\int_0^{T}F_{cont}(t)e^{\left(\frac{-2jk\pi t}{\mathscr{T}}\right)}dt \tag{65}$$

The linear system assumption indicates that the response of one linear system under a summation set of harmonics equals the summation of its response to each harmonic individually [25]. In this way, the electromechanical response of MPB for harmonic excitation in Eq. (58) and Eq. (59) is used to predict the harvester's response to individual harmonics. So, the normalized steady-state voltage expression for the case of harmonic excitation force is given by

$$V_s(\omega)=\frac{v_s(\omega,t)}{\mathbb{F}e^{j\omega t}}=\left(\frac{-\sum_{i=1}^{\infty}\frac{j\vartheta_i\omega\phi_i(x)|_{x=\frac{L_{up}}{2}}}{-\omega^2+2j\xi_i\omega_i\omega+\omega_i^2}}{j\omega C_p+\frac{1}{R}+\sum_{i=1}^{\infty}\frac{j\vartheta_i^2\omega}{-\omega^2+2j\xi_i\omega_i\omega+\omega_i^2}}\right) \tag{66}$$

The absolute steady-state periodic voltage based on the truncated Fourier series, taking N harmonic pairs, can be expressed as

$$|v(t)|\cong\sum_{k=-N}^{N}\left|V_s\left(\frac{2k\pi}{\mathscr{T}}\right)e^{\left(\frac{2jk\pi t}{\mathscr{T}}\right)}C_k\right| \tag{67}$$

In Section 5.2, specific instruction is provided for determining the appropriate number of harmonic pairs (N).

The calculated steady-state voltage and displacement expressions can be utilized to define the input mechanical energy and the generated electrical output energy within each period:

$$E_{input}=\int_0^{\mathscr{T}}F_{cont}(t).dw|_{x=L_{up}/2}(t) \tag{68}$$

$$E_{output}=\int_0^{\mathscr{T}}\frac{v(t)^2}{R_l}dt \tag{69}$$

Here, $w|_{x=L_{up}/2}(t)$ denotes the transverse displacement of the MPB at $x=L_{up}/2$. Note that the input energy in Eq. (68) includes two factors: the contact force function, and the displacement of the applied force point. Moreover, energy conversion efficiency (ECE) is defined in Eq. (70) to represent the conversion efficiency from input mechanical

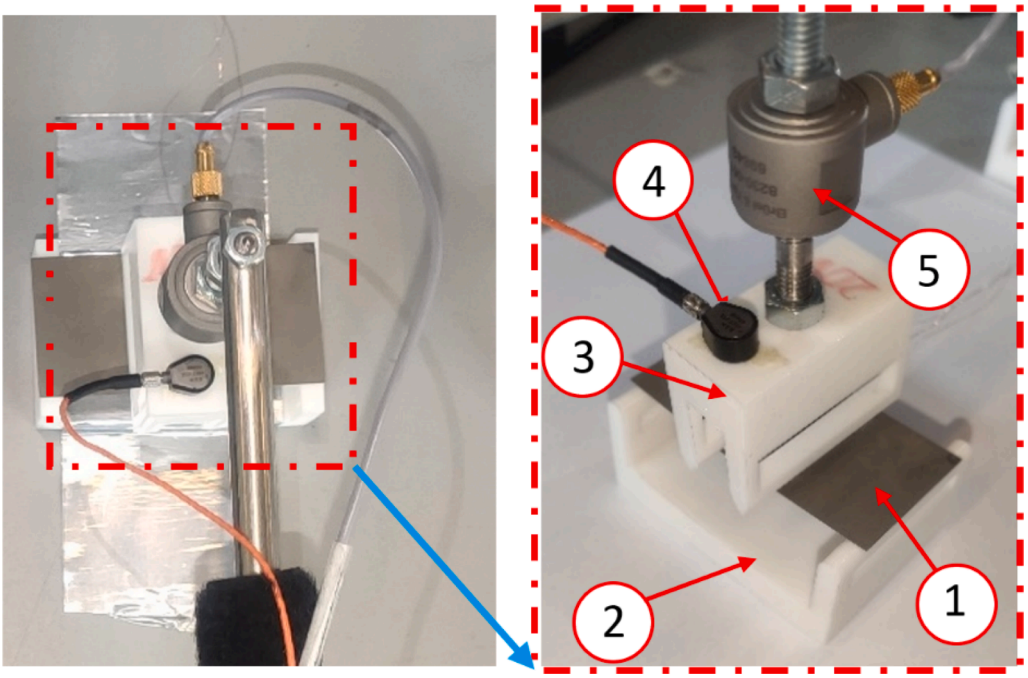

Fig. 5. The experimental setup for the four-point bending test: (1) piezoelectric patch, (2) bottom clamp, (3) upper clamp, (4) accelerometer sensor, and (5) force transducer sensor.

Table 1
The electromechanical characteristics of the MPB.

Characteristics	Substrate (Brass)	Piezoceramic (PZT-5A)
Mass density [kg/m^3]	$\rho_s = 8300$	$\rho_p = 7750$
Elastic modulus [GPa]	$E_s = 105$	$c_{11}^E = 61$
Substrate thickness [mm]	$h_s = 0.13$	$h_p = 0.19$ (each)
Piezoelectric constant [C/m^2]	—	$\overline{e}_{31} = -10.4$
Permittivity constant [nF/m]	—	$\overline{\varepsilon_{33}}s = 13.3$
Beam length [mm]	$L_b = 63.5$	
Beam width [mm]	$b = 31.8$	

energy to output electrical energy.

$$ECE = \frac{E_{output}}{E_{input}} \times 100\% \tag{70}$$

3.2.4. The time-dependent response for arbitrary non-periodic excitation (numerical analysis)

In addition to the Laplace method described in section 3.2.2, numerical methods (e.g., Runge–Kutta) are extensively used for solving ODEs. In this regard, Eq. (28) and Eq. (29) can be transformed into first-order differential equations for the application of numerical methods in a state-space representation. Although continuous vibration systems have infinite eigenfrequency, the expansions may be truncated to consider only effective modes. This work takes into account the four primary vibration modes as

$$\begin{bmatrix} \mathscr{X}_1(t) \\ \mathscr{X}_2(t) \\ \mathscr{X}_3(t) \\ \mathscr{X}_4(t) \\ \mathscr{X}_5(t) \\ \mathscr{X}_6(t) \\ \mathscr{X}_7(t) \\ \mathscr{X}_8(t) \\ \mathscr{X}_9(t) \end{bmatrix} = \begin{bmatrix} q_1(t) \\ \dot{q}_1(t) \\ q_2(t) \\ \dot{q}_2(t) \\ q_3(t) \\ \dot{q}_3(t) \\ q_4(t) \\ \dot{q}_4(t) \\ v(t) \end{bmatrix} \tag{71}$$

According to Eq. (28) and Eq. (29), it can be rewritten as

Table 2
The comparison of predicted natural frequencies by the developed model against COMSOL Multiphysics.

Natural Frequency	Developed model (Hz)	COMSOL Multiphysics			
		Without electrostatic effect (Hz)	Error (%)	With electrostatic effect (Hz)	Error (%)
First	160.31	160.26	0.03	161.36	0.65
Second	1442.8	1441.2	0.11	1451.1	0.57
Third	4007.7	3997.4	0.26	4024.9	0.43
Forth	7855.2	7817.0	0.49	7871.3	0.20

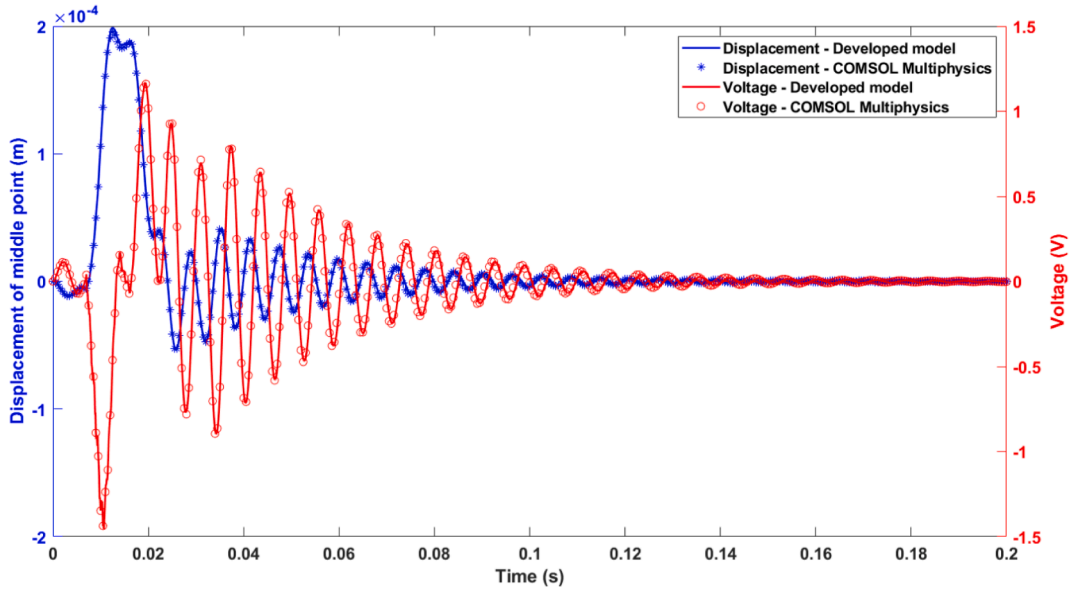

Fig. 6. The voltage and beam middle point's displacement – developed model and COMSOL Multiphysics.

$$\begin{bmatrix} \dot{\mathscr{X}}_1(t) \\ \dot{\mathscr{X}}_2(t) \\ \dot{\mathscr{X}}_3(t) \\ \dot{\mathscr{X}}_4(t) \\ \dot{\mathscr{X}}_5(t) \\ \dot{\mathscr{X}}_6(t) \\ \dot{\mathscr{X}}_7(t) \\ \dot{\mathscr{X}}_8(t) \\ \dot{\mathscr{X}}_9(t) \end{bmatrix} = \begin{bmatrix} \mathscr{X}_2(t) \\ f_{c1}(t) - 2\xi_1\omega_1\mathscr{X}_2(t) - \omega_1^2\mathscr{X}_1(t) + \theta_1\mathscr{X}_9(t) \\ \mathscr{X}_4(t) \\ f_{c2}(t) - 2\xi_2\omega_2\mathscr{X}_4(t) - \omega_2^2\mathscr{X}_3(t) + \theta_2\mathscr{X}_9(t) \\ \mathscr{X}_6(t) \\ f_{c3}(t) - 2\xi_3\omega_3\mathscr{X}_6(t) - \omega_3^2\mathscr{X}_5(t) + \theta_3\mathscr{X}_9(t) \\ \mathscr{X}_8(t) \\ f_{c4}(t) - 2\xi_4\omega_4\mathscr{X}_8(t) - \omega_4^2\mathscr{X}_7(t) + \theta_4\mathscr{X}_9(t) \\ 1/C_p[-\mathscr{X}_9(t)/R - (\theta_1\dot{\mathscr{X}}_2(t) + \theta_2\dot{\mathscr{X}}_4(t) + \theta_3\dot{\mathscr{X}}_6(t) + \theta_4\dot{\mathscr{X}}_8(t))] \end{bmatrix} \tag{72}$$

In contrast to steady-state response FRFs, the numerical method considers the initial conditions $w(x,0) = w_0(x)$, $\dot{w}(x,0) = \dot{w}_0(x)$, and $v(0) = v_0$. Hence, these initial conditions in modal coordinates can be given as

$$q_i(t=0) = \int_{-L_b/2}^{L_b/2} w_0(x) m \phi_i(x) dx \tag{73}$$

$$\dot{q}_i(t=0) = \int_{-L_b/2}^{L_b/2} \dot{w}_0(x) m \phi_i(x) dx \tag{74}$$

$$v(t=0) = v_0 \tag{75}$$

The result of the implemented state-space is presented in section 5.1.1.

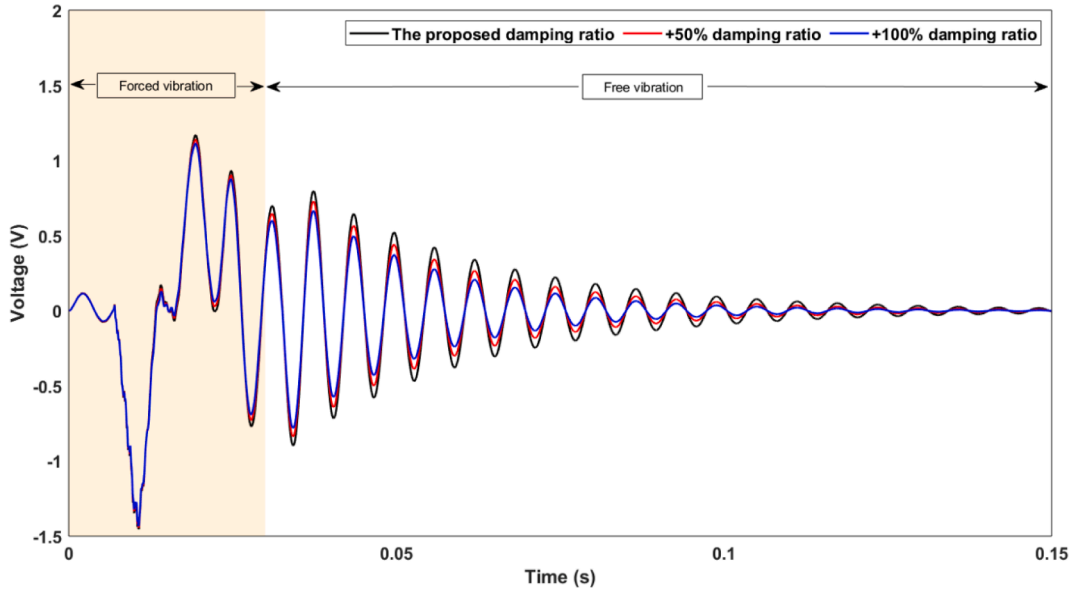

Fig. 7. The voltage response in terms of different damping ratios.

4. Experimental setup

Experimental measurements are used for validation of the developed model, with the setup shown in Fig. 5. The upper clamp is placed on the tip of an impulse hammer so that the force transducer (Bruel and Kjaer, type 8230–001) measures the real-time hammer force. The measured force comprises the applied contact force to MPB and the inertia force of the upper clamp. Therefore, an accelerometer (Bruel and Kjaer, type 4517–002) is mounted on the upper clamp to assess the clamp's inertia force for the determination of contact force as

$$\vec{F}_{cont}(t) = \vec{F}_{trans}(t) - \vec{F}_{inertia}(t) \tag{76}$$

The piezoelectric patch's output is connected to an electrical impedance, here a purely resistive load. The impedance voltage, accelerometer, and force transducer signals are transmitted into a data analyzer (Bruel and Kjaer, type 3677-A-041).

As shown in Fig. 5, the bottom clamp is fixed to a flat surface while it holds the MPB on two supports. A lubricant is employed to minimize coulomb friction between MPB and clamps so that the constraint can be considered as a roller support approximately. The electromechanical characteristics of the MPB are presented in Table 1.

5. Results and discussions

|In first, the developed model is validated against experimental and FEM results. Then, the validated model is studied to observe the effects of parameters under different excitations, including single impact and periodic excitation. In addition, it is discussed regarding optimal parameter arrangement for providing the best performances. Finally, the FPB-EH is compared with the cantilever configuration.

5.1. Validation of the developed model

The model verification is accomplished by extensive comparisons of the developed analytical model's results with outputs from commercial finite element software and various experimental data points at different force levels and boundary conditions. Since the piezoelectric energy harvester is an electromechanical Multiphysics model, the validating parameters cover both the mechanical/vibration parameters and the electrical outputs, ensuring that the model is valid for energy harvester mechanical design and also the performance evaluation.

5.1.1. Validation of the developed model with FEM model

According to Fig. 4, the FEM model is set up in COMSOL Multiphysics to compare the natural frequencies and the transient response of the MPB under a single impact. The FEM geometric and material properties are given in Table 1.

Regarding the mechanical parameter validation, first, Table 2 compares the natural frequencies of the developed model (Eq. (52)) against COMSOL Multiphysics. The COMSOL FEM model computes the natural frequencies of the FPB-EH with $L_d = L_b$ in Table 2, with and without considering the piezoelectric effect. Since natural frequencies are the most prominent design parameter in piezoelectric harvesters, the natural frequencies of up to four vibration modes are compared. There is an excellent agreement between the developed model and FEM output, even with the electrostatic effect, indicating that the natural frequency has a negligible dependency on the electrostatic effect. The error of the identified natural frequency for the first four bending modes is below 0.7%. The higher-mode natural frequency agreement ensures the multi-mode analysis accuracy.

A single impact force during contact time is experimentally measured, as described in Fig. 5, and imported into both the developed model and the COMSOL FEM model. Importing experimental force data leads to a more realistic analysis by considering actual contact force even though the nonlinear contact analysis effect is not present. As an instance, an impact force with amplitude 1.06 N and acting time 0.025 sec is taken from one experimental test. The state-space method studies the transient solution under this measured contact force in Fig. 6.

Fig. 6 presents the mechanical response (beam's middle-point displacement) and the electrical response (voltage) under the real-time measured impact excitation. The comparison is between the state-space solution of the analytical model and the commercial COMSOL results. There are several small-amplitude fluctuations at $0 < t < 0.02$ s in voltage and displacement responses, which are due to fluctuations in the recorded experimental contact force. After the impact hit, the piezoelectric beam starts free vibration based on its natural frequencies. Overall, the deflection and voltage diminish over time due to the damping. The impact effect lasts for approximately 0.15 s.

The COMSOL and state-space transient solution agree with good accuracy. The presented model is also in agreement with the small-amplitude transition fluctuations. As a result, it is concluded that the developed model can compute the displacement and voltage of the MPB without need for further FEM confirmation.

In this study, the proportional damping coefficients of the piezoelectric patch were determined based on the material datasheet [27] and experimental analysis. According to the material datasheet, the first-mode quality factor is $\Omega = 80$. This quality factor is used for other vibration modes as suggested due to the lack of damping data [28]. Having the quality factors for modal modes, mass proportional damping (a_0) and stiffness proportional damping (a_1) coefficients can be calculated by Eq. (77) [28]. In addition, the agreement between experimental and model results in subsection 5.1.2 indicates that the proposed damping ratio leads to appropriate voltage estimations, so the damping model is valid.

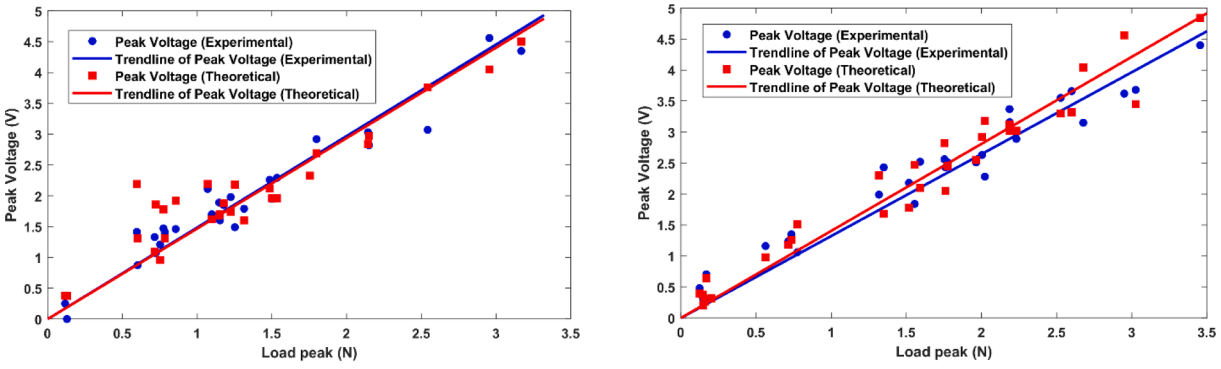

Fig. 8. The experimental and theoretical peak voltage variation under different contact forces corresponding to (a) $L_{up} = 20$mm, and (b) $L_{up} = 40$mm.

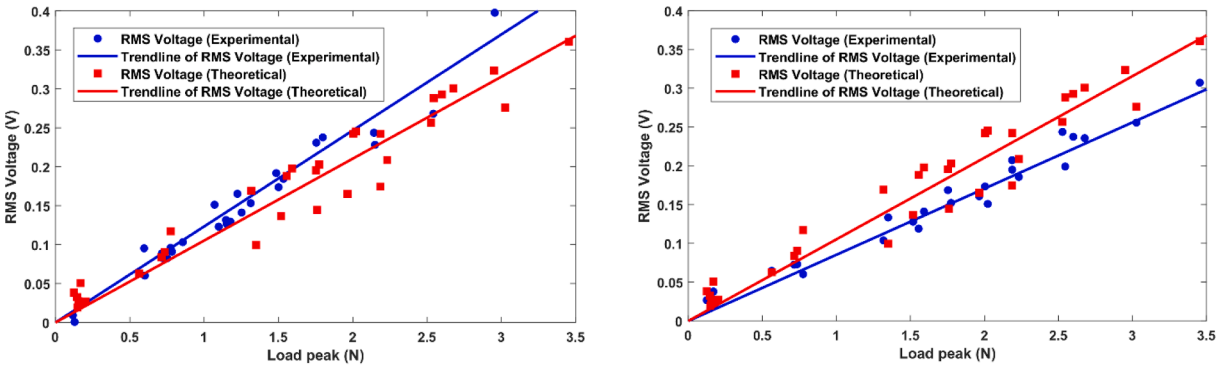

Fig. 9. The variation of experimental and theoretical RMS voltage (within 1 sec) under different contact forces corresponding to (a) $L_{up} = 20$mm, and (b) $L_{up} = 40$mm.

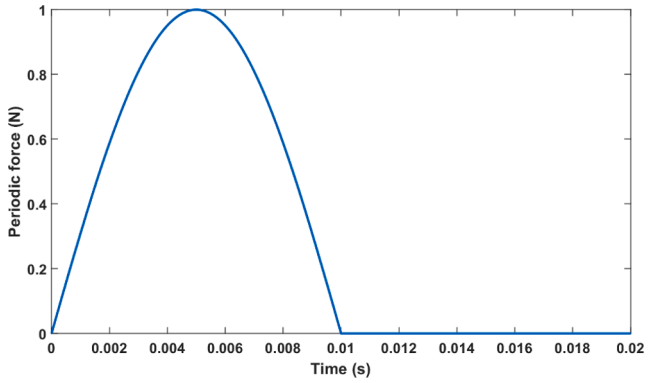

Fig. 10. The periodic force based on half sinusoidal pulse.

$$\begin{Bmatrix} a_0 \\ a_1 \end{Bmatrix} = \frac{2\xi}{\omega_m + \omega_n} \begin{Bmatrix} \omega_m \omega_n \\ 1 \end{Bmatrix} \tag{77}$$

which $\xi = \frac{1}{2\zeta}$ and m and n are two arbitrary mode numbers

The model solution depends on damping coefficients based on equations (59) and (60). Mainly, the damping ratio affects the response in the vicinity of natural frequencies. The effect of damping is considerable in free vibration response due to the dependency of the free vibration response on the natural frequencies. Moreover, the damping effect in forced response is noticeable if the applied contact force comprises considerable harmonics close to the harvester's natural frequencies [29]. Otherwise, the damping effect is not remarkable in the forced response of a single impact, and the force response of this FPB-EH is a significant part of output voltage.

To evaluate the damping effect, Fig. 7 illustrates the system's response under previous impact force with different damping coefficients. The response is made of a forced response (0 to 0.03 s), where the upper clamp is in contact with the harvester, and a free vibration response, after applying the impact force. The effect of damping is small in the forced vibration region since the harmonics in the applied impact force are away from the harvester's natural frequencies. However, the free vibration response is considerably affected by the damping ratio.

5.1.2. *Validation of the developed model with experimental results*

The described experimental setup in section 5.1.1 is studied under single-impact excitations while $L_d = L_b = 63$ mm and the FPB-EH is connected to the electrical resistance of 2.3 kΩ. For this evaluation, two upper clamps are considered with different length $L_{up} = 20$mm and $L_{up} = 40$mm. Several arbitrary impact forces (with different amplitudes and

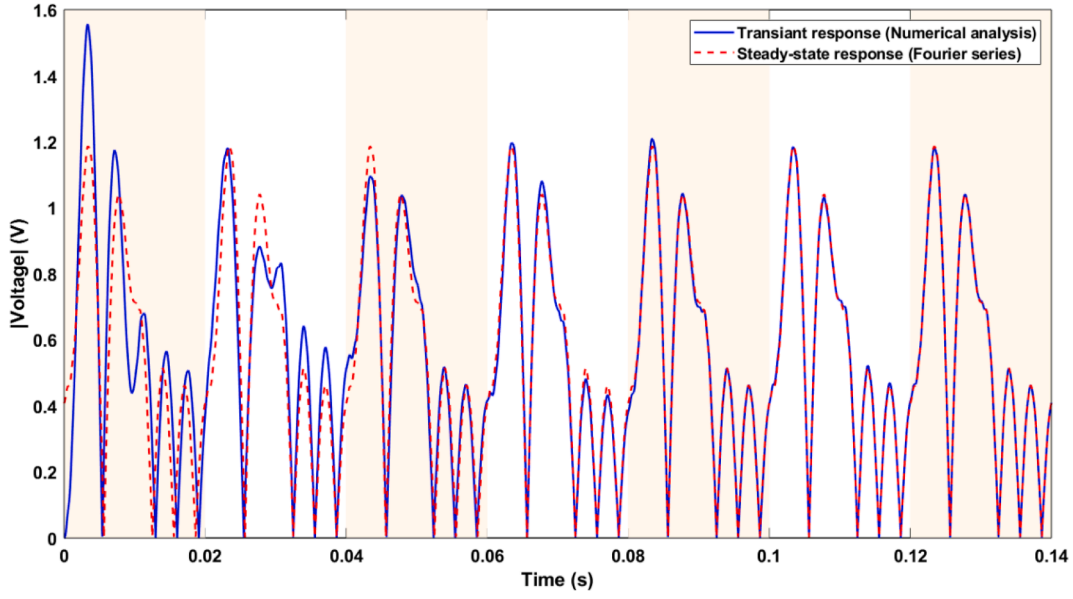

Fig. 11. The transient and steady-state responses per the half sinusoidal periodic excitation in 7 cycles.

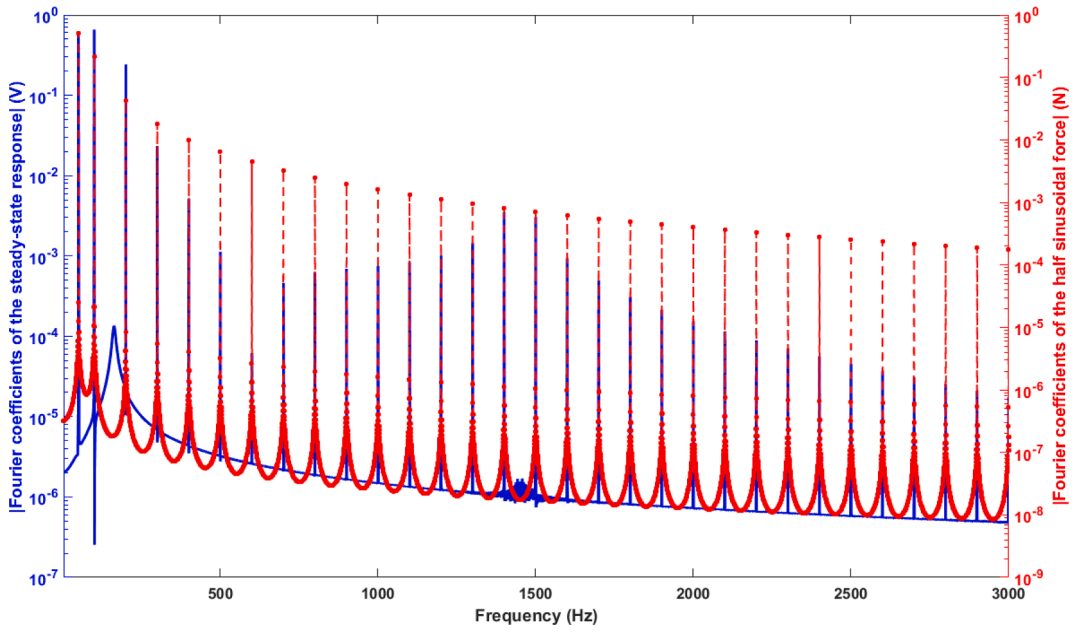

Fig. 12. The Fourier coefficients of the harmonics associated with the steady-state voltage response and the applied contact load.

Table 3
The Fourier coefficients of contact force and steady-state voltage at non-zero frequency.

Frequency pairs (Hz)	Fourier coefficients	
	Contact force (N)	Steady-state voltage (V)
50	0.5000	0.5764
100	0.2122	0.6562
200	0.0424	0.2417
300	0.0182	0.0233
400	0.0101	0.0051
500	0.0064	0.0011

time history) were applied to the MPB. The peak voltage output corresponding to two clamps with $L_{up} = 20$mm and $L_{up} = 40$mm are plotted against the peak impact force in Fig. 8-a and Fig. 8-b, respectively. The experimental data indicate an approximately linear correlation between peak force and peak voltage. There are some scatters due to variations in the duration of impact force acting time; since the hammer impact is controlled by hand, the impact acting time can be different. Therefore, impact forces with an identical peak force and different acting times could lead to different peak voltages.

The counterpart measured experimental contact force was imported into the state-space model to compute the numerical response of harvester. The transient model of subsection 3.2.4 calculates the peak voltage associated with each contact force. Since actual force waveforms with different acting times are imported, the peak voltage in numerical solutions can also be scattered. Therefore, two trendlines are included to facilitate a comparison of the developed model and the experimental

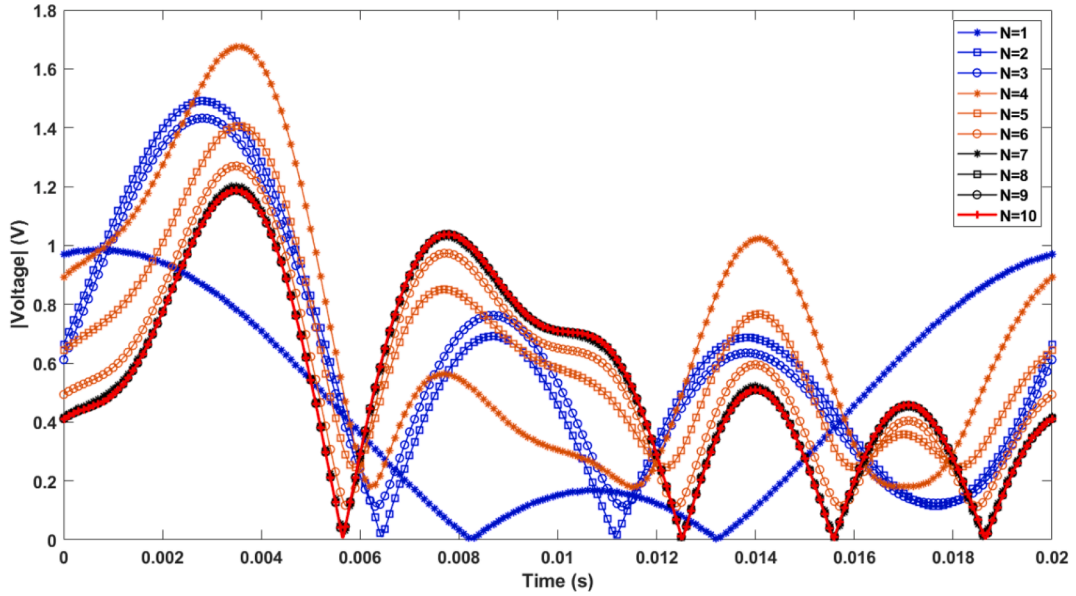

Fig. 13. The steady-state response per the half sinusoidal based on different N.

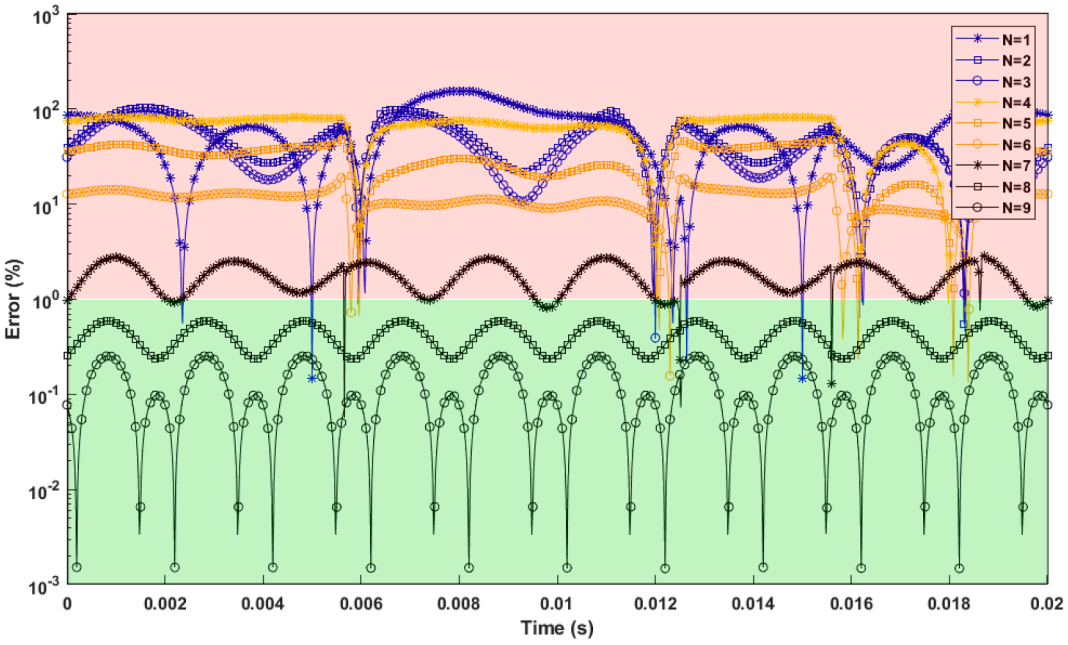

Fig. 14. The effect of harmonic pairs (N) on computational error within one period-time.

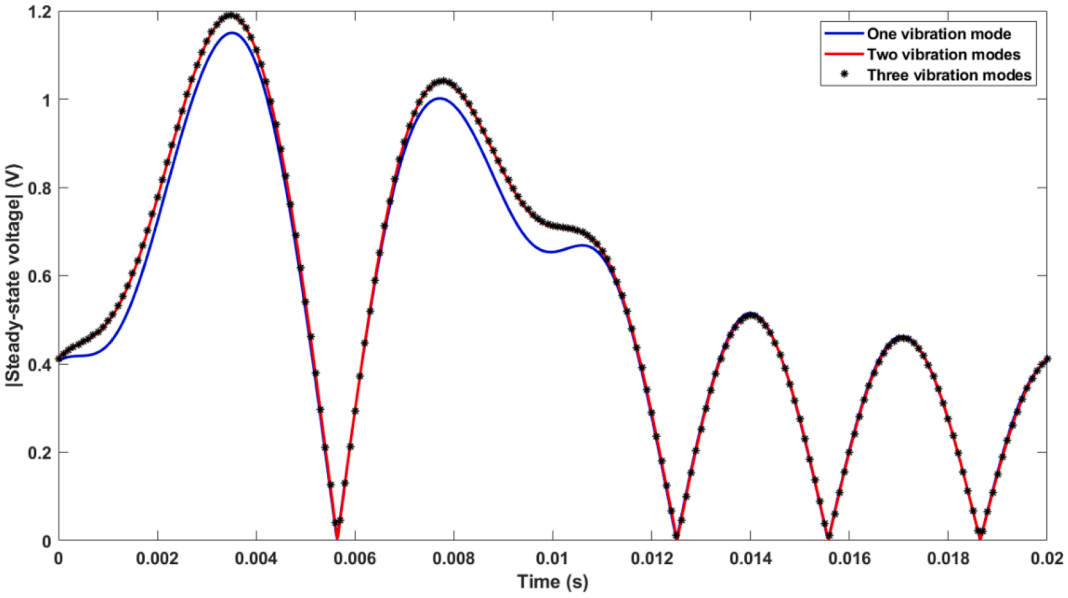

Fig. 15. The effect of vibration mode number on steady-state response per the half sinusoidal contact force.

data. This comparison indicates that the proposed model can evaluate the peak voltage under different contact forces with reasonable accuracy. The discrepancy between theoretical and experimental results emanates from statistical and random factors in applying force by the impact hammer.

In addition to peak voltage, the RMS voltage is examined under single-impact excitations based on two mentioned different upper clamps. The experimental and theoretical RMS voltages corresponding to the clamps with $L_{up} = 20\text{mm}$ and $L_{up} = 40\text{mm}$ are presented in Fig. 9-a and Fig. 9-b, respectively. There is good agreement between the experimental and model results, both at data points and with the trendlines. The model discrepancy is slightly more significant for the RMS than for the peak analysis. The possible roots can be the proper damping estimation and the boundary condition perfectness. Note that the boundary condition and damping effects can be prominent in the transient response, as shown in Fig. 7.

After the model verification based on single impacts, the analyses of FPB-EH response under more complicated force excitations are presented in the following sections.

5.2. *The steady-state response under periodic contact force*

The previous section studied FPB-EH response under single impact force, while energy harvesters usually encounter repeated excitations in practice. This section explores the transient and steady-state response of the MPB under more general periodic excitation. For illustration, a half sinusoidal periodic excitation force with a period-time $\mathscr{T} = 0.02\text{s}$ is defined as an instance of the contact force, as shown in Fig. 10.

The transient voltage response represented in Eq. (72) under the proposed periodic force is shown in Fig. 11 while geometrical

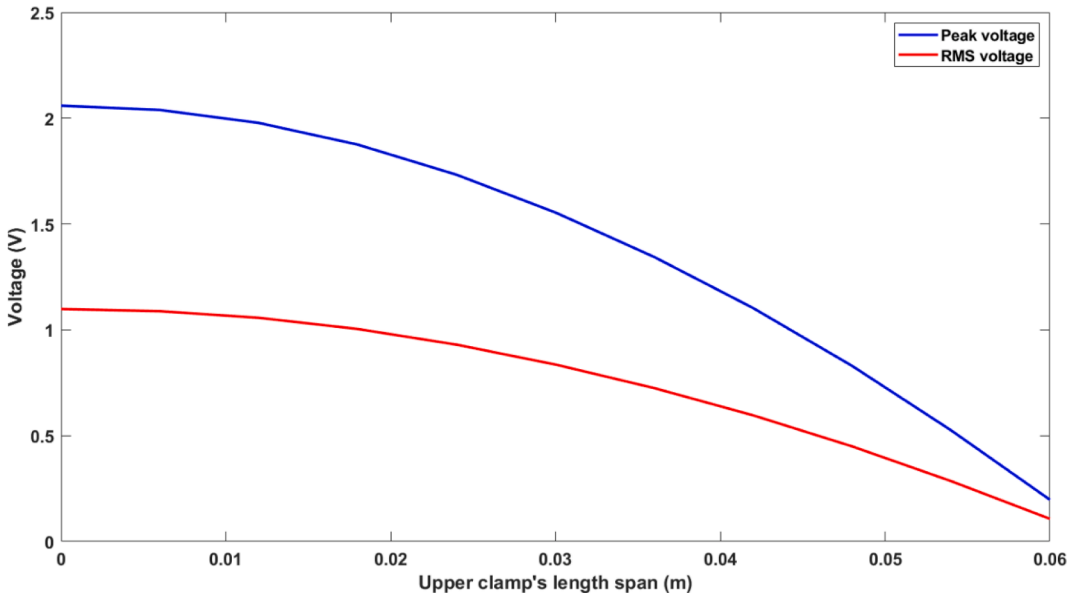

Fig. 16. The peak and RMS voltage during one period-time at different upper clamp's length spans.

parameters are $L_d = L_b = 63\,\text{mm}$ and $L_{up} = 20\,\text{mm}$ and the electrical resistance is 2.3 kΩ. Note that the initial conditions were considered to be zero. Moreover, the steady-state response from Eq. (67) is presented in Fig. 11 to compare with the transient response. This comparison shows that the transient response converges to the steady-state response after about six cycles due to eliminating homogeneous response by damping. Note that this decaying cycle number can differ depending on the harvester's damping coefficient.

The steady-state response in Fig. 11 is for N = 200 and four bending vibration modes. As mentioned, two parameters significantly affect the Fourier Transform's steady-state response: the number of harmonic pairs (N), and the number of vibration modes included in the model. A high number of mentioned variables guarantees a more exact solution, but the computational time becomes significant. Thus, selecting proper numbers is a trade-off between the solution exactness and computation time. The following paragraphs guide these parameter selections.

The highest harmonic frequency of the Fourier expansion $\left(\frac{2N\pi}{\mathcal{T}}\right)$ should be correlated with the applied contact force's primary harmonics. For a more detailed explanation, the Fourier coefficients of the applied load (Fig. 10) and the harvester's steady-state voltage response (Fig. 11) are presented in Fig. 12. The main frequency pairs of the applied contact force are 50, 100, 200, 300, 400, and 500 Hz. Note that 50-Hz corresponds to the input force period (0.02 s). Moreover, the principal Fourier coefficients of applied load and voltage response in these frequencies are summarized in

Table 3. Note that for the half-sine case study, the contact force Fourier coefficients decrease with frequency while the voltage response Fourier coefficients are not consistently descending; for instance, the second pair of Fourier coefficients is the largest.

In the following, an instruction is suggested to determine the harmonic pairs (N) and vibration modes for a generic periodic contact force.

1. Find the highest Fourier coefficients of contact force (FCCF) associated with the frequency ω^*, which is denoted as FCCF(ω^*).

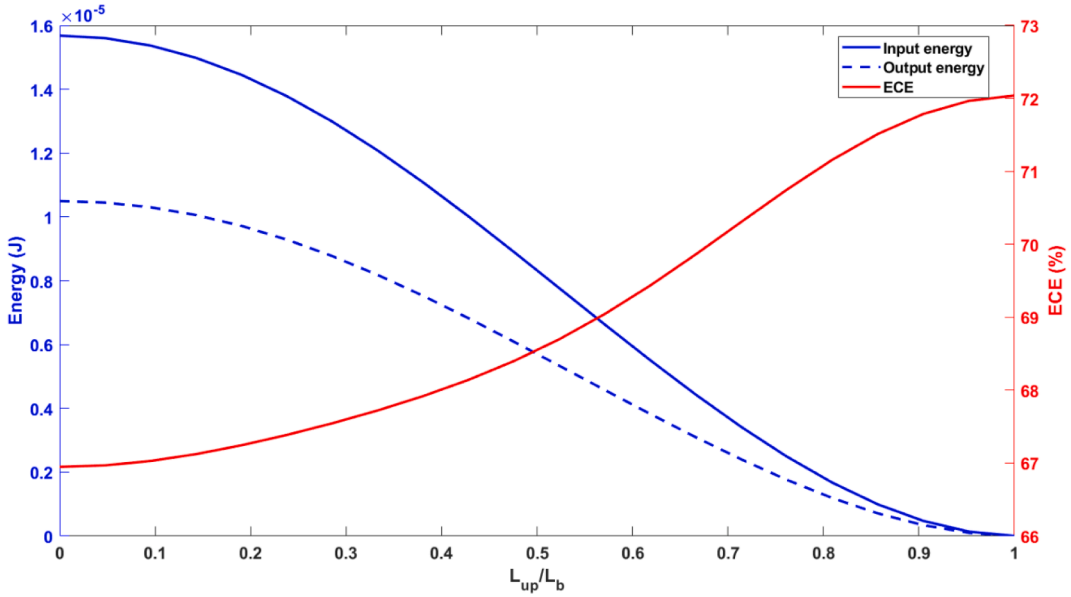

Fig. 17. The input and output energies along with ECE during one period-time at different upper clamp's length spans.

2. Find the truncating frequency ($\omega_{\text{tru.}}$) that FCCF($\omega_{\text{tru.}}$) > FCCF(ω^*)/Λ, where Λ is the amplitude factor for tuning the smallest value of the Fourier coefficients. Higher Λ passes small-valued Fourier coefficients in the voltage response, leading to a more accurate response.
3. Determine the least natural mode (in Eq. (66)) with a frequency higher than $\omega_{\text{tru.}}$ is evaluated.
4. The number of harmonic pairs in Eq. (67) can be evaluated by $N \geq (\mathscr{T}\omega_{\text{tru.}}/2\pi)$.
5. Supplementary step: In some situations, some harmonics are not covered due to resolution limitations in the Fourier transform [30]. Therefore, it is suggested that the time sample is increased to more than $\mathscr{T}$ to enhance resolution.

For instance, this instruction is implemented into the current analysis as follows: Step 1- the FCCF($\omega^* = 50\text{Hz} \times 2\pi$) equals 0.5 N; Step 2- Inserting $\Lambda = 50$, the FCCF(ω^*)/ Λ equals 0.01 N, so $\omega_{\text{tru.}} = 400Hz \times 2\pi$; Step 3- the second natural mode associated with frequency 1442.8 Hz is selected. Step 4- Finally, it is determined that $N = 8$.

In this regard, the shown periodic voltage response in Fig. 11 is re-evaluated based on the different values of N in Fig. 13 to observe the effect of this parameter. This figure implies that the voltage response is converged with $N = 8$.

For a more detailed and quantitative observation, an error factor is defined as follows.

$$Error_i(t) = \frac{|V_{N=i}(t) - V_{N=\mathscr{M}}(t)|}{|RMS(V_{N=\mathscr{M}})|} \times 100(\%) \tag{78}$$

The parameter $\mathscr{M}$ represents the number of harmonic pairs associated with a high-order model as a reference case to present the relative error bound. The defined error factor is computed for described cases N = 1 ~ 9 (in Fig. 13) with $\mathscr{M} = 10$, which is illustrated in Fig. 14. In this figure, the maximum allowed error level is considered 1%, which separates the error axis into two regions to distinguish desirable error levels (in green) from desirable error levels (in red). Therefore, the results indicate that the selected truncation number through the above-mentioned instruction (N = 8) is sufficient for errors lower than 0.8%. Nevertheless, the higher values for N can lead to better accuracy but with higher computation time.

The effect of the number of vibration modes is presented in Fig. 15 to test the effect of mode numbers. The voltage comparisons prove that the voltage response does not change significantly for more than two bending modes. The remaining results presented in this article consider five primary vibration modes to encompass comprehensive conditions.

This subsection also demonstrates the instruction for time-efficient and accurate calculation of the harvester's output. The computation time with $N = 8$ and two primary vibration modes (in Fig. 15) is remarkably faster than the manually setting with $N = 200$ and five primary vibration modes. This setting is used for future numerical studies because of its time efficiency and accuracy.

5.3. Parametric study

This section examines the steady-state response to investigate the effect of parameters associated with the contact force and the harvester's geometry. This parameter study is accomplished in several steps, and each step is complementary to the previous step(s). At first, the harvester's output is evaluated per different upper clamp's span (subsection 5.3.1). It is expected that the harvester's outputs are affected drastically by variation of this parameter due to the dependency location of applying contact force to this parameter. Later, the proposed harvester is studied under contact forces with different waveforms to be determined the best waveform based on different aspects (subsection 5.3.2). Next, the effect of the best force waveform's period time is investigated to study the harvester's outputs per different excitation frequencies, especially frequency bandwidth (subsection 5.3.3). The following steps determine the optimal condition for FPB-EH, leading to the best output power and energy conversion efficiency.

5.3.1. The effect of upper clamp's span on MPB output

The half sinusoidal contact force represented in Fig. 10 is applied with different upper clamp spans to evaluate peak and RMS voltages, as shown in Fig. 16. In this study, the geometrical parameters are $L_d = L_b =$ 63 mm and the electrical resistance is 2.3 kΩ. Decreasing the L_{up} value increases the peak and RMS voltages, e.g., the maximum peak and RMS voltage outputs occur at$L_{up} = 0$, which are 2.06 V and 1.1 V, respectively. Note that$L_{up} = 0$ is the special case that the contact force is applied on the harvester middle line, where four-point bending becomes three-point bending.

In addition to the peak and RMS voltages, the ECE is an essential factor that specifies the harvester's performance. In this regard, the input energy, output energy, and ECE versus the nondimensional upper

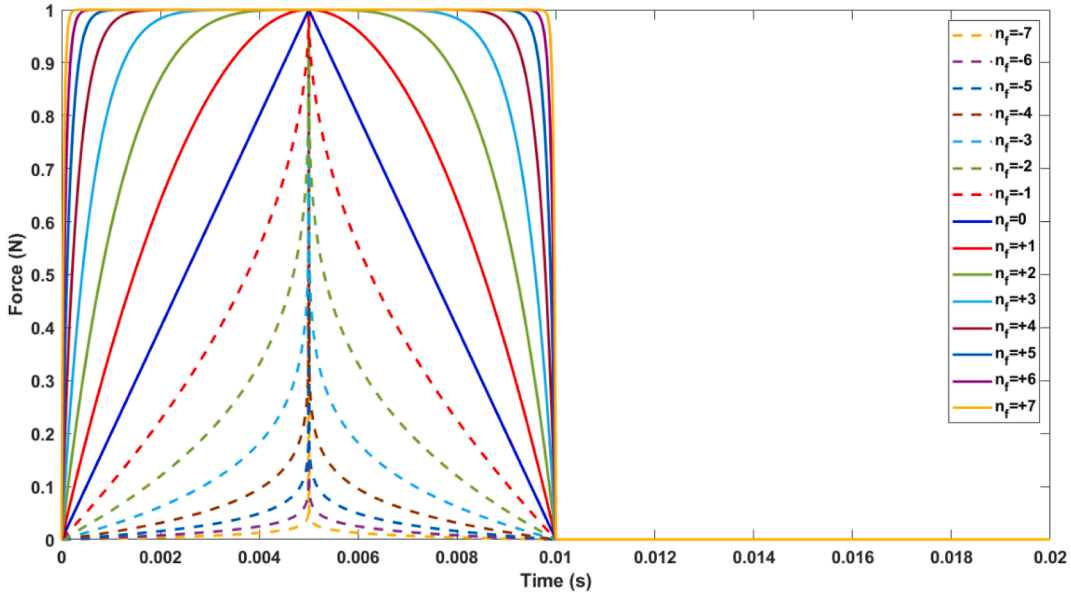

Fig. 18. The different waveforms of contact force with a constant period-time 0.02 s.

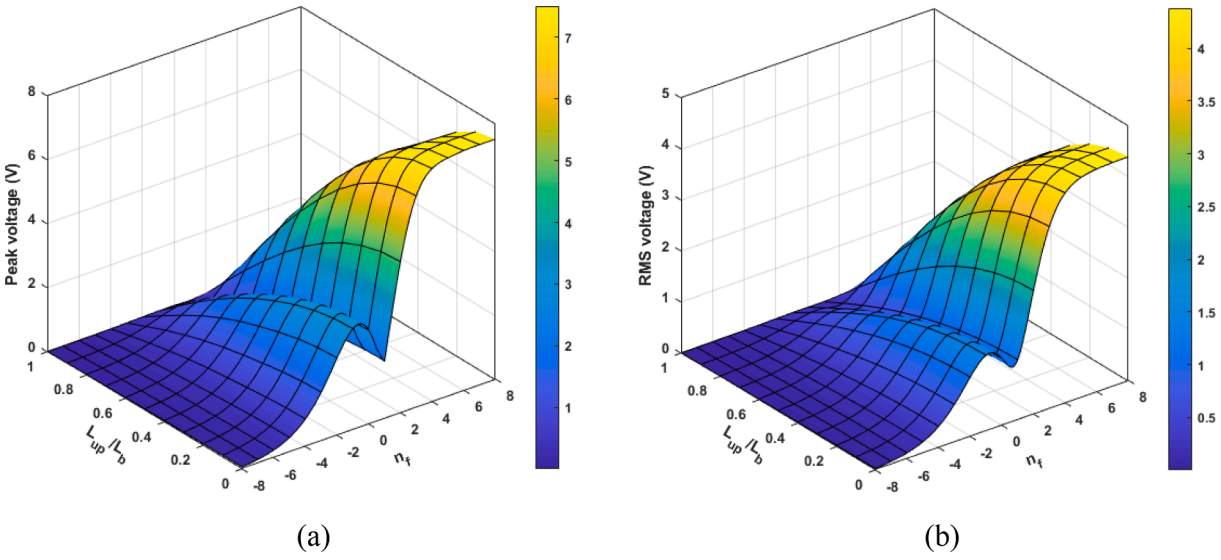

Fig. 19. The variation of Peak voltage and RMS voltage per different n_f and L_{up}/L_b.

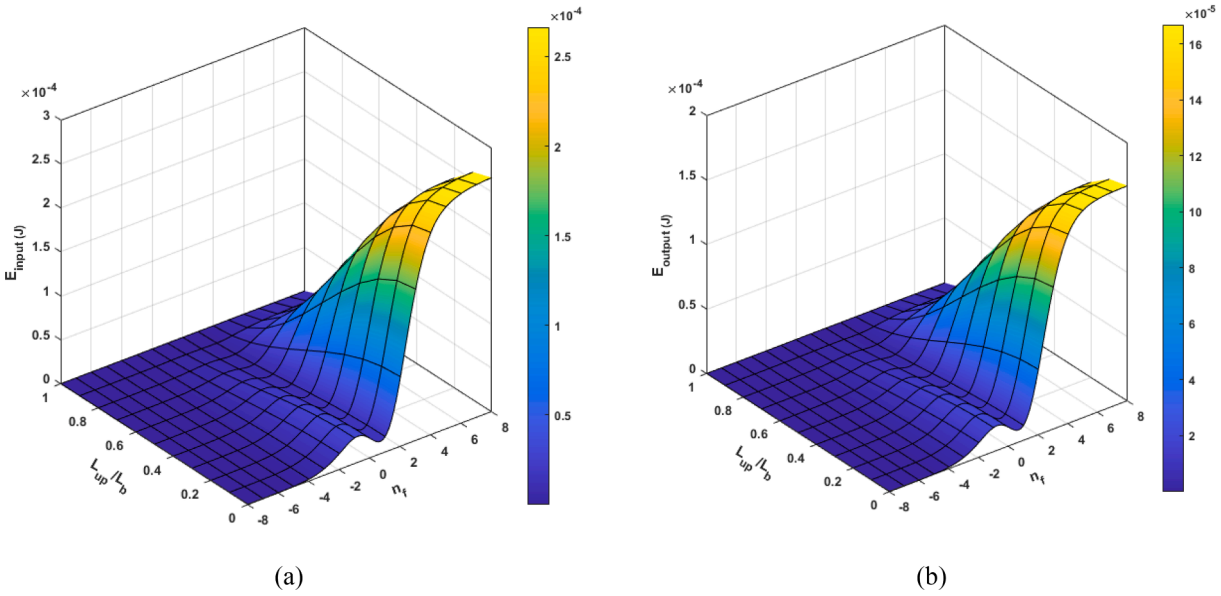

Fig. 20. The variation of (a) input and (b) output energies versus n_f and L_{up}/L_b.

clamp span are shown in Fig. 17. As discussed in subsection 3.2.3, in addition to the output energy, the input energy also depends on the input force function and harvester system response. The results indicate that even though output energy for $L_{up}/L_b = 0$ is maximum, this condition presents the lowest ECE. Note that the contact force is directly resisted by the bottom clamp when $L_{up}/L_b = 1$, and no mechanical deformation and energy are applied to the harvester, e.g., E_{input}=0. In this regard, the presented results throughout this paper consider that L_{up}/L_b approaches to unit value, and the $L_{up}/L_b = 1$ condition is neglected.

In summary, as the location of applying contact force becomes closer to the beam's end edge, the ECE improves from 67% to 72%. As the property $L_{up}\rightarrow 0$ the harvester's vibration amplitude increases. As a result, the higher amplitude vibration can increase dissipated energy by damping, which underlies decreasing ECE.

5.3.2. *The effect of contact force's waveform*

The contact force can be considered based on different waveforms. This section evaluates the waveform of contact force for the energy harvester with the geometrical and electrical configuration in the previous subsection. Practically, the contact force is dictated by the vibration source, but the contact force can be tuned by the design and integration of the energy harvester to the vibration source.

A half-cycle unit force function with period-time $\mathscr{T}$ given by Eq. (79) is defined to mimic a periodic impact contact force.

$$F_{cont}(t) = \begin{cases} 1 - \left|\dfrac{t - \mathscr{T}/4}{\mathscr{T}/4}\right|^{2^{n_f}} & 0 < t \le \mathscr{T}/2 \\ 0 & \mathscr{T}/2 < t \le \mathscr{T} \end{cases} \tag{79}$$

The proposed force function is illustrated in Fig. 18 for various n_f values. The contact waveform around$n_f = 1$ resembles the half-sine impact. Positive n_f waveforms approach to the square-wave impact force, while the negative n_f waveforms approach to the ideal Dirac impact waveform.

The Peak and RMS voltages versus force waveforms and upper clamp span are shown in Fig. 19. The RMS voltage variation is similar to the

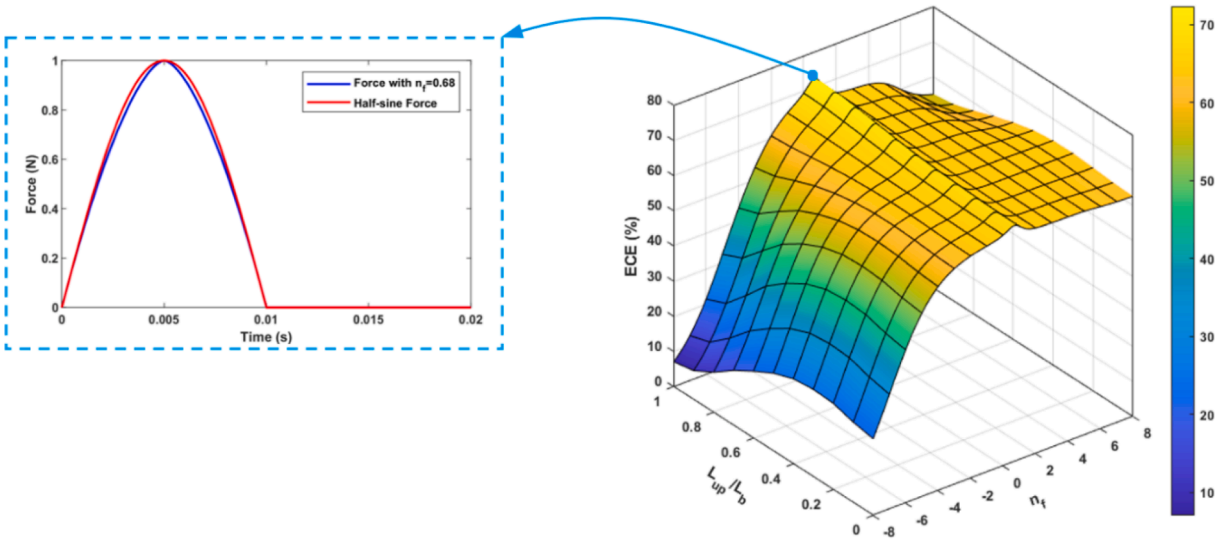

Fig. 21. The variation ECE versus n_f and L_{up}/L_b along with comparison between the optimal force with $n_f = 0.68$ and half-sine one.

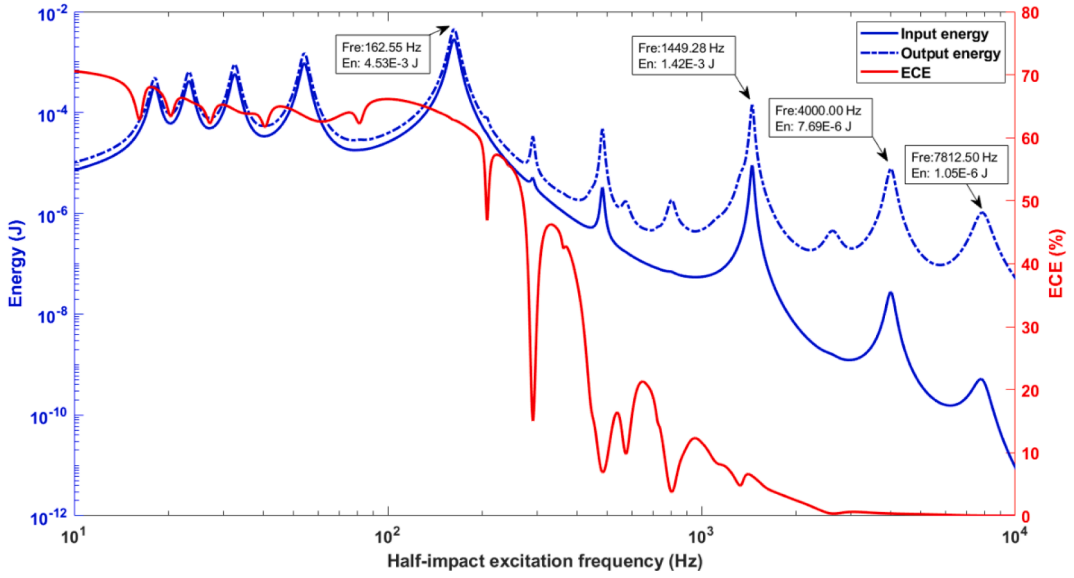

Fig. 22. The input and output energies along with ECE during one period-time at different contact force frequencies.

Table 4
The comparison of bandwidth of MPB under harmonic and half-sine excitations.

Excitation type	f_L(Hz)	f_P(Hz)	f_H(Hz)	ABW (Hz)	FBW (%)
Harmonic	160.52	162.55	164.58	4.06	2.5
Half-sine	157.15	162.55	167.95	10.8	6.65

input energy pattern. The results indicate that as n_f and L_{up}/L_b approach ∞ and 0, respectively, the Peak and RMS voltages increase to their global maximum values. Indeed, the Peak and RMS voltages on the line $L_{up}/L_b = 0$ converge for $n_f \geq 5$. This result can be linked to the higher impact force power for higher n_f. Overall, the highest Peak and RMS voltages among the accomplished analyses are 7.4 V and 4.38 V, respectively.

In addition to the global extremum, local extrema can be of interest as they relate to the contact force waveform. There are local extrema between $-1<n_f<1$, e.g., the relative minimum Peak and RMS voltages appear at $n_f = 1$ and $n_f = 0.69$, which equals 1.785 V and 1.062 V, respectively. Moreover, the relative maximum Peak and RMS voltages are 3.233 V and 1.494 V, which appear at $n_f = -0.6$ and $n_f = -0.77$, respectively.

Similarly, the input and output energies versus force waveforms and upper clamp span are shown in Fig. 20-a and -b. These energies are derived from one period-time in the steady-state condition, as represented in Eq. (68) and (69). The overall patterns are similar to those of peak and RMS voltages.

Furthermore, some local extremums exist within $-1<n_f<1$. The relative maximum and minimum of input energy in line $L_{up}/L_b = 0$ occur at $n_f = -0.78$ and $n_f = +0.69$, which are equal to 3.016×10^{-5} J and 1.463×10^{-5} J, respectively. However, the locations of relative maximum and minimum output energy are in compliance with RMS

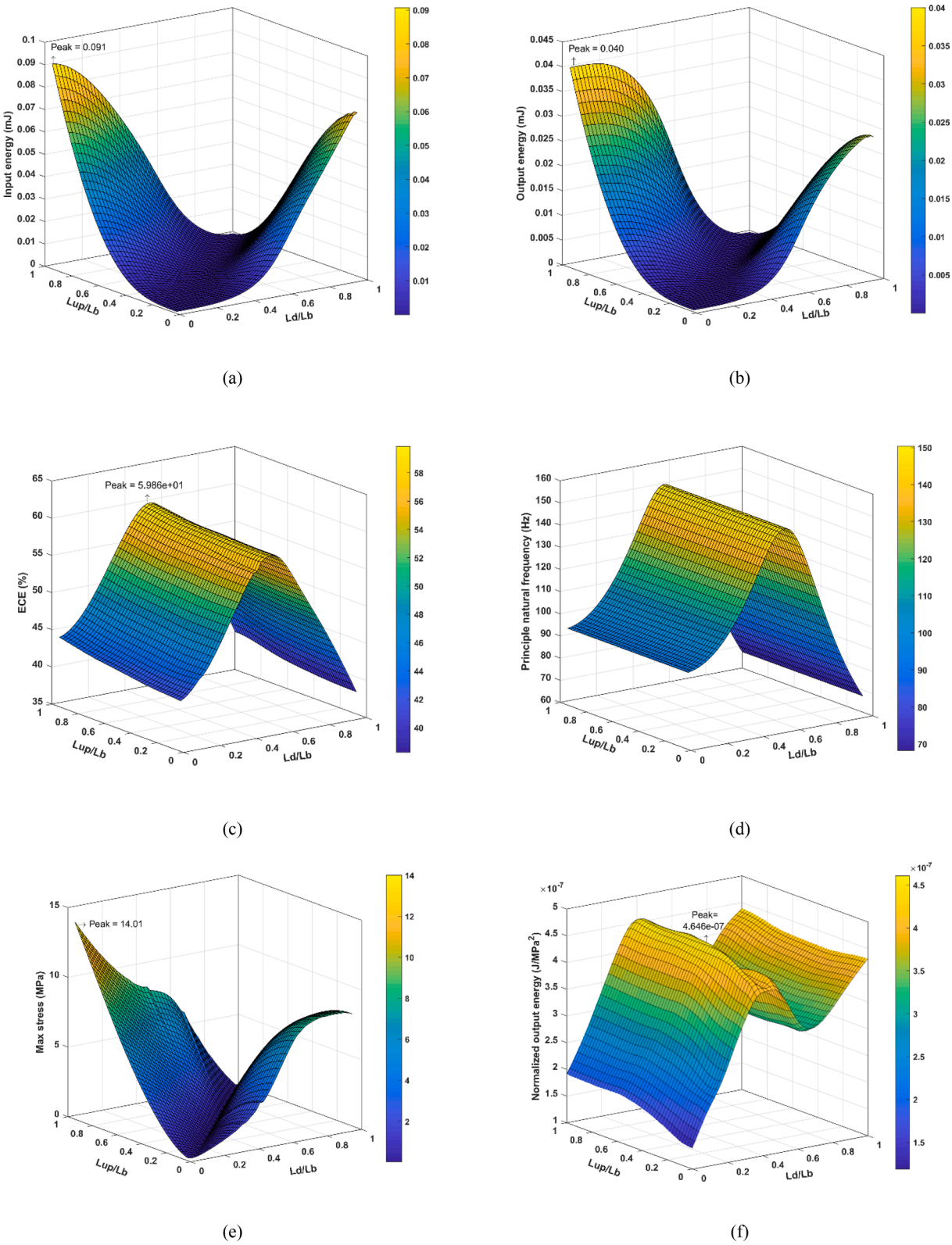

Fig. 23. The variation of FPB configuration's outputs under different ratios L_d/L_b and L_{up}/L_b: (a) input energy, (b) output energy, (c) ECE, (d) principal natural frequency, (e) maximum stress, and (f) normalized output energy.

voltage, and their values are equal to 1.944×10^{-5} J and 9.822×10^{-6} J, respectively.

As mentioned, the ECE expression helps to find the best condition for conversion efficiency. Although the pattern of input and output energies are similar, the ECE evaluates the relative variation of these energies in detail, as shown in Fig. 21. The absolute maximum ECE occurs in the line with $n_f = 0.68$. The ratio L_{up}/L_b also affects the ECE so that the maximum ECE is 72.3% in the condition $L_{up}/L_b = 1$ and $n_f = 0.68$.

The resemblance between the optimal waveform setting $n_f = 0.68$ and the half-sine waveform is also shown in Fig. 21. This suggests that

the half-sine waveform is the best periodic half waveform in terms of energy conversion efficiency.

5.3.3. The effect of contact force's period-time

In the previous sections, the proposed impact force's period-time was considered as the constant value 0.02 s. This section explores the effect of contact force's period-time on MPB's performance. It was shown that the optimal periodic waveform force is in accordance with $n_f = 0.68$; this can also be approximated by the half-sine waveform. The excitation frequency for general periodic forces can be defined as $Fre = 1/\mathscr{T}$.

The MPB configuration has $L_{up}/L_b = 0$ and is subjected to an impact force with $n_f = 0.68$ and different *Fre*. The input energy, output energy, and ECE versus half-sine impact excitation frequency are presented in Fig. 22. The bending resonant frequencies are shown in boxes in Fig. 22. The first four bending natural frequencies considering electrostatic and electrical load effects become 162.55, 1449.28, 4000, and 7812.5 Hz. The input and output energies have extrema when the frequency of half-sine impact force is equal to each resonant frequency. The maximum input and output energies appear at the MPB's 1st natural frequency, $Fre = \omega_1$, and the energy conversion efficiency below the 1st natural frequency remains high. However, the energy conversion efficiency in higher modes decreases significantly due to the cancelation voltage phenomenon.

In addition to the bending modes, there are four peaks before the first natural frequency. These frequencies are at $\omega_1/9$, $\omega_1/7$, $\omega_1/5$, and $\omega_1/3$, fractions of the first natural frequency (162.55 Hz). Indeed, the proposed contact force comprises harmonics with frequencies higher than *Fre* (as Table 3), so these harmonics can be matched with the principal natural frequency, which leads to significant power generation. Similarly, there are four peak points between the first and second natural frequencies, including 290.023 Hz ($\omega_2/5$), 483.092 Hz ($\omega_2/3$), 572.082 Hz ($\omega_3/7$) and 802.568 Hz ($\omega_3/5$). Note that this phenomenon does not exist for pure harmonic excitation. The low-frequency peaks are of great interest for low-frequency energy harvesting, enabling effective electrical energy generation at frequencies below the 1st natural frequency.

Furthermore, the frequency bandwidth is calculated in Table 4 based on Fig. 22. In addition to conventional absolute frequency bandwidth (ABW), the fractional bandwidth (FBW) expresses relative frequency bandwidth in dimensionless form as [3]

$$FBW = \frac{f_H - f_L}{f_P} \times 100 \tag{80}$$

Table 4 indicates that the half-sine impact excitation improves the ABW and FBW of the harvester by 166% compared to the harmonic excitation by exciting a broader range of frequencies. Therefore, regarding the broadband energy conversion, the impact type force is preferable since the half-sine impact force gives 6.65% fractional bandwidth. This conclusion is regardless of the boundary condition; thus, it is valid for the cantilever or four-point bending beams. Nevertheless, the half-sine impact force is easier to apply using the FPB configuration; by tuning the upper clamp to any vibration source, impact force can be applied to the MPB.

5.4. Comparison with traditional cantilever configuration in the aspect of normalized energy

The presented results in the previous section considered the simplified condition $L_b = L_d$. This section considers the variation of L_d/L_b to produce a range of behavior between FPB and cantilever configurations. Note that, unlike the cantilever configuration, the FPB configuration provides a flexible boundary condition so that the harvester's natural frequency can be tuned by controlling the roller support locations (L_d). However, the cantilever configuration is fixed and ineffective for natural frequency tuning for specific harvester shapes and geometry. Thus, the FPB configuration is tunable for a wide range of excitation forces.

A specific MPB (as described in Fig. 2 and Table 1) with length $L_b =$ 10 cm is used to fairly compare an FPB-EH with a cantilever harvester. The both configurations are studied under half-sine excitation with force amplitude 0.1 N and the period $\mathscr{T} = 2\pi/\omega_1$ (where ω_1 is the first natural frequency in either FPB or cantilever beams). This eliminates the non-matching effect of contact force frequency with the principal natural frequency of the harvester.

The energies, mechanical and electrical outputs of the FPB-EH under different ratios L_d/L_b and L_{up}/L_b are shown in Fig. 23. Fig. 23-a and Fig. 23-b indicate that the input and output energies within one period have two extremum situations: (I) when $L_d/L_b = 1$ and $L_{up}/L_b \underrightarrow{0}$ (the impact force is on the middle line of the harvester while beam length equals bottom clamp length), and (II) $L_d/L_b \underrightarrow{0}$ and $L_{up}/L_b = 1$ (the bottom clamp is in the harvester middle line and upper clamps at the harvester outer edges). The extremum situation II provides absolute maximum output energy, which is 0.040 J per 0.1 N half-sine impact. The variation of ECE is represented in Fig. 23-c, which shows that the ECE is maximized (59.86%) on $L_d/L_b = 0.52$ regardless of L_{up}/L_b. Similarly, Fig. 23-d reveals that the principal natural frequency of the harvester becomes maximal around this line, which indicates a direct relation between ECE and principal natural frequency. Indeed, this conformity implies that the maximum ECE occurs approximately when the harvester's principal natural frequency is maximized.

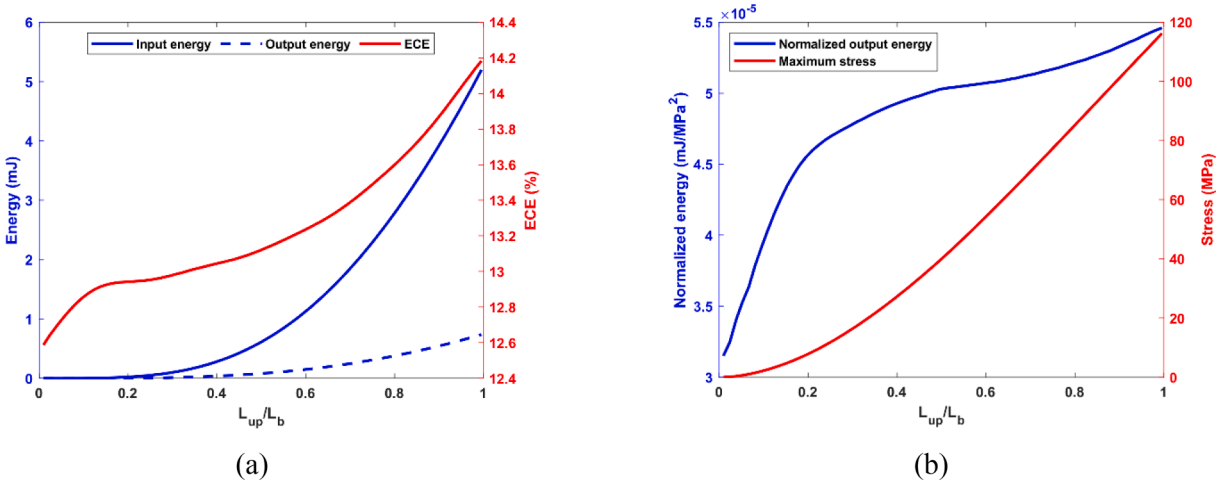

Fig. 24. The cantilever configuration's outputs under different ratios L_{up}/L_b: (a) input and output energies along with ECE, (b) normalized energy and maximum stress.

Table 5
The outputs of cantilever and four-point bending configurations based on a specific MPB.

Configuration	Critical cases		Output energy (mJ)	ECE (%)	NOE (J/MPa^2)
	L_d/L_b	L_{up}/L_b			
Cantilever	N.A*	1	**0.737**	14.18	0.546e−7
FPB	0.06	0.97	**0.040**	44.53	2.28e−7
	0.52	0.97	0.025	**59.86**	4.03e−7
	0.42	0.47	0.002	57.07	**4.65e−7**

* Not applicable.

In addition, the maximum longitudinal stress (MLS) over one force period time is depicted in Fig. 23-e. The MLS correlates closely with the trend of input and output energies. Two extremum situations of MLS are according to the input/output energies. The harvester's fatigue life, especially due to the piezoelectric layer's brittleness, is expected to be sensitive to the applied maximum stress [31]. Thus, a harvester performance criterion, the normalized output energy (NOE), is defined as the output energy per squared maximum stress, given by:

$$NOE = \frac{E_{output}}{\mathrm{MLS}^2} \tag{81}$$

The NOE is a durability parameter of the energy harvester; higher NOE means higher energy harvester performance per unit of stress. The NOE is illustrated in Fig. 23-f. The maximum NOE occurs for $L_d/L_b = 0.42$ and $L_{up}/L_b = 0.47$, so this configuration can be interpreted as the best condition for a trade-off between the harvester's performance and durability. Note that the best durability configuration demonstrates a reasonably good ECE (see Fig. 23-c). Generally, a good balance of energy efficiency and durability can be achieved by $0.42 < L_d/L_b < 0.52$ and $L_{up}/L_b = 0.47$.

Similarly, the cantilever configuration is examined, and the input/output energies and ECE are shown in Fig. 24-a. Moreover, the maximum stress and normalized output energy (NOE) are shown in Fig. 24 (b). Note that the L_d/L_b parameter is not applicable for the cantilever configuration, and L_{up} is the distance of the applied load from the fully clamped line. These results indicate the peak values of stress, ECE, input, output, and normalized energies appear at $L_{up}/L_b = 1$.

The foremost results for the cantilever and FPB configurations are summarized in Table 5. The cantilever harvester generates 0.737 mJ energy, providing considerably higher output energy than the FPB with 0.04 mJ. However, the FPB configuration presents remarkable ECE and normalized output energy, which are 322.1% and 751.6% more than the cantilever type, respectively. By combining the output energy and ECE comparisons, the cantilever generates higher energy but with low ECE, meaning that the material is inefficiently employed.

The weaknesses and strengths of each configuration were explored comprehensively. In summary, the cantilever configuration is preferable in certain conditions: (I) when the mechanical input energy is ample, in other words, the ECE is not critical, and (II) when the period time of the excitation is constant, which allows frequency matching. However, the FPB configuration is desirable in the following conditions: (I) when the mechanical input energy is scarce or the allocated space for the harvesting system is limited, so ECE becomes a consideration, and (II) when the harvester's fatigue life is of great importance, for instance, in remote locations where maintenance is not straightforward, and (III) when the excitation force period is variable; then the FPB-BC flexibility by roller-supports is applicable for matching the harvester's principal frequency to the variable excitation frequency through an active controller mechanism.

6. Conclusion and future works

This research comprehensively investigated the four-point bending (FPB) configuration for piezoelectric energy harvesting, contrasting it to the conventional cantilever type. First, an electromechanical model was developed to present frequency response functions (FRFs) for the FPB energy harvester (FPB-EH). This model considers two mode-shape functions for internal and external sections, extending the model's applicability to a wide range of cases. The governing ordinary differential equations were transformed into a state-space representation to study the transient system response for non-periodic excitation. In addition, the developed FRFs and Fourier series method were utilized to present the steady-state response of FPB-EH under arbitrary periodic excitations. The model was validated against COMSOL and experimental results under various excitations. After validation, a parametric study was performed to investigate the effects of clamps span, force waveform, and period-time of contact force. As a result, it was shown that the FPB-EH under the periodic half-impact excitation with $n_f = 0.68$ provides the maximum ECE (72.3%) with $L_{up}/L_b = 1$, which is optimal for situations with low mechanical input energy. Furthermore, the half-sine impact improved the bandwidth ABW and FBW of the harvester by 166% more than the harmonic sinusoidal force. The results indicate that the FPB configuration significantly enhances both energy conversion efficiency and normalized output energy by 322% and 638%, respectively. Lastly, the FPB configuration was compared with the cantilever energy harvester to reveal the weaknesses and strengths of both configurations. The cantilever type is favorable for working conditions with constant force period-time, no limitation regarding input energy, and low priority of the harvester's fatigue life. However, the FPB configuration is suitable for high priority for the harvester's fatigue life, high ECE, and possible changes in the period-time of excitation force.

These future works are recommended for further investigations in this research field: The clamp surface shape might play a significant role in the contact force, while the flat clamp shape is exclusively used in this research. Moreover, the material of the upper clamp affects the frequency and waveform of applied force, which can be considered an effective factor in adapting the harvester for different situations. In addition, the geometric nonlinearity effects due to large deformations and prestressed situations can be a noticeable phenomenon that changes the harvester's response.

CRediT authorship contribution statement

Milad Hasani: Methodology, Writing – original draft, Software, Data curation, Visualization, Software. **Majid Khazaee:** Conceptualization, Methodology, Software, Data curation, Investigation. **John E. Huber:** Conceptualization, Methodology, Investigation. **Lasse Rosendahl:** Methodology, Supervision. **Alireza Rezania:** Methodology, Investigation, Supervision.

Declaration of Competing Interest

The authors declare that they have no known competing financial interests or personal relationships that could have appeared to influence the work reported in this paper.

Data availability

Data will be made available on request.

Acknowledgments

This work is supported by a research grant from the Lundbeck, LF-Experiment grant, under grant number R324-2019-1747. Moreover, this research is partially financed by the Independent Research Fund Denmark International Post-doc grant under grant number 1031-00001B, and Danish Cardiovascular Academy, which is funded by the Novo Nordisk Foundation, grant number NNF20SA0067242, and Danish Heart Foundation.

References

[1] Tang X, Wang X, Cattley R, Gu F, Ball AD. Energy harvesting technologies for achieving self-powered wireless sensor networks in machine condition monitoring: a review. Sensors (Basel) 2018;18. 10.3390/s18124113.
[2] Khazaee M, Rosendahl L, Rezania A. Online condition monitoring of rotating machines by self-powered piezoelectric transducer from real-time experimental investigations. Sensors 2022;22:3395.
[3] Hasani M, Irani RM. The optimization of an electromagnetic vibration energy harvester based on developed electromagnetic damping models. Energy Convers Manag 2022;254:115271. https://doi.org/10.1016/j.enconman.2022.115271.
[4] Pan Y, Zuo L, Ahmadian M. A half-wave electromagnetic energy-harvesting tie towards safe and intelligent rail transportation. Appl Energy 2022;313:118844. https://doi.org/10.1016/j.apenergy.2022.118844.
[5] Zargari S, Rezania A, Daie Z, Veladi H, Sobhi J. Nano energy effect of the inherent capacitance optimization on the output performance of triboelectric nanogenerators. Nano Energy 2022;92:106740. https://doi.org/10.1016/j.nanoen.2021.106740.
[6] Zhu M, Zhang J, Wang Z, Yu X, Zhang Y, Zhu J, et al. Double-blade structured triboelectric–electromagnetic hybrid generator with aerodynamic enhancement for breeze energy harvesting. Appl Energy 2022;326:119970. https://doi.org/10.1016/j.apenergy.2022.119970.
[7] Daqaq MF, Masana R, Erturk A, Dane QD. On the role of nonlinearities in vibratory energy harvesting: a critical review and discussion. Appl Mech Rev 2014;66:040801. https://doi.org/10.1115/1.4026278.
[8] Salmani H, Rahimi G, Saraygord Afshari S. Optimization of the shaping function of a tapered piezoelectric energy harvester using tabu continuous ant colony system. J Intell Mater Syst Struct 2019:1045389X1987339. 10.1177/1045389X19873391.
[9] Fu X, Liao W-H. Nondimensional model and parametric studies of impact piezoelectric energy harvesting with dissipation. J Sound Vib 2018;429:78–95. https://doi.org/10.1016/j.jsv.2018.05.013.
[10] Abdelkefi A, Barsallo N. Nonlinear analysis and power improvement of broadband low-frequency piezomagnetoelastic energy harvesters. Nonlinear Dyn 2016;83:41–56. https://doi.org/10.1007/s11071-015-2306-8.
[11] Nie X, Tan T, Yan Z, Yan Z, Hajj MR. Broadband and high-efficient L-shaped piezoelectric energy harvester based on internal resonance. Int J Mech Sci 2019;159:287–305. https://doi.org/10.1016/j.ijmecsci.2019.06.009.
[12] Fan Y, Ghayesh MH, Lu T-F. A broadband magnetically coupled bistable energy harvester via parametric excitation. Energy Convers Manag 2021;244:114505. https://doi.org/10.1016/j.enconman.2021.114505.
[13] Harne RL, Zhang C, Li B, Wang KW. An analytical approach for predicting the energy capture and conversion by impulsively-excited bistable vibration energy harvesters. J Sound Vib 2016;373:205–22. https://doi.org/10.1016/j.jsv.2016.03.012.
[14] Meirovitch L. Fundamentals of vibrations. McGraw-Hill; 2001.
[15] Khazaee M, Huber JE, Rosendahl L, Rezania A. Four-point bending piezoelectric energy harvester with uniform surface strain toward better energy conversion performance and material usage. J. Sound Vib. Mar. 2023;548:117492. https://doi.org/10.1016/j.jsv.2022.117492.
[16] Khazaee M, Rezaniakolaei A, Rosendahl L. A broadband Macro-Fiber-Composite piezoelectric energy harvester for higher energy conversion from practical wideband vibrations. Nano Energy 2020;76:104978.
[17] Kim S-W, Lee T-G, Kim D-H, Lee K-T, Jung I, Kang C-Y, et al. Determination of the appropriate piezoelectric materials for various types of piezoelectric energy harvesters with high output power. Nano Energy 2019;57:581–91.
[18] Chen K, Fang S, Gao Q, Zou D, Cao J, Liao WH. An enhanced nonlinear piezoelectric energy harvester with multiple rotating square unit cells. Mech Syst Signal Process 2022;173:109065. https://doi.org/10.1016/j.ymssp.2022.109065.
[19] Chen K, Fang S, Gao Q, Zou D, Cao J, Liao WH. Enhancing power output of piezoelectric energy harvesting by gradient auxetic structures. Appl Phys Lett 2022;120. https://doi.org/10.1063/5.0082015.
[20] Yeo HG, Trolier-McKinstry S. Effect of piezoelectric layer thickness and poling conditions on the performance of cantilever piezoelectric energy harvesters on Ni foils. Sensors Actuators, A Phys 2018;273:90–7. https://doi.org/10.1016/j.sna.2018.02.019.
[21] Zhou S, Lallart M, Erturk A. Multistable vibration energy harvesters: Principle, progress, and perspectives. J Sound Vib 2022;528. https://doi.org/10.1016/j.jsv.2022.116886.
[22] Chen L, Liao X, Sun B, Zhang N, Wu J. A numerical-experimental dynamic analysis of high-efficiency and broadband bistable energy harvester with self-decreasing potential barrier effect. Appl Energy 2022;317:119161. https://doi.org/10.1016/j.apenergy.2022.119161.
[23] Chen K, Gao F, Liu Z, Liao WH. A nonlinear M-shaped tri-directional piezoelectric energy harvester. Smart Mater Struct 2021;30. https://doi.org/10.1088/1361-665X/abe87e.
[24] Xia Y, Pang J, Yang L, Chu Z. Investigation on clearance-induced vibro-impacts of torsional system based on Hertz contact nonlinearity. Mech Mach Theory 2021;162:104342. https://doi.org/10.1016/j.mechmachtheory.2021.104342.
[25] Erturk A, Inman DJ. Piezoelectric energy harvesting. Wiley; 2011.
[26] Ogata K. Modern control engineering. 5th ed. Pearson; 2010.
[27] Richard Kensley (www.piezo.com). PSI catalog; 2012.
[28] Clough RW, Penzien J. Dynamics of structures 2015.
[29] He J, Fu Z-F. Modal analysis. 1st ed. Butterworth-Heinemann; 2001.
[30] Kanatov I, Kaplun D, Butusov D, Gulvanskii V, Sinitca A. One technique to enhance the resolution of discrete fourier transform. Electronics 2019;8:330. https://doi.org/10.3390/electronics8030330.
[31] Salazar R, Serrano M, Abdelkefi A. Fatigue in piezoelectric ceramic vibrational energy harvesting: a review. Appl Energy 2020;270:115161. https://doi.org/10.1016/j.apenergy.2020.115161.